Differential Activity-Dependent Scaling of Synaptic Inhibition and Parvalbumin Interneuron Recruitment in Dentate Projection Neuron Subtypes

Milad Afrasiabi[1], Akshay Gupta[1,2], Huaying Xu[3], Bogumila Swietek[1] and Vijayalakshmi Santhakumar[1,2]

[1]Department of Pharmacology, Physiology and Neuroscience, Rutgers New Jersey Medical School, Newark, New Jersey 07103, [2]Department of Molecular, Cell and Systems Biology, [2]Department of Statistics, University of California Riverside, Riverside, California 92521.

Word count for Abstract: 199

Pages: 52 (with figures and supplement) Number of figures: 7

Supplementary Figures: 5 Tables: 0 Supplementary Tables: 4

Correspondence:

Vijayalakshmi Santhakumar, PhD
Department of Molecular, Cell and Systems Biology
University of California, Riverside
3401 Watkins Drive (Rm 1308 Spieth Hall) Riverside, CA 92521
E-mail: vijayas@ucr.edu

Abstract:

Strong inhibitory synaptic gating of dentate gyrus granule cells (GCs), attributed largely to fast-spiking parvalbumin interneurons (PV-INs), is essential to maintain sparse network activity needed for dentate dependent behaviors. However, the contribution of PV-INs to basal and input driven sustained synaptic inhibition in GCs and semilunar granule cells (SGCs), a sparse morphologically distinct dentate projection neuron subtype are currently unknown. We find that although basal inhibitory postsynaptic currents (IPSCs) are more frequent in SGCs and optical activation of PV-INs elicited IPSCs in both GCs and SGCs, optical suppression of PV-INs failed to reduce IPSC frequency in either cell type. Amplitude and kinetics of IPSCs evoked by perforant path activation were not different between GCs and SGCs. However, the robust increase in sustained polysynaptic IPSCs elicited by paired afferent stimulation was lower in SGCs than in simultaneously recorded GCs. Optical suppression of PV-IN selectively reduced sustained IPSCs in SGCs but not in GCs. These results demonstrate that PV-INs, while contributing minimally to basal synaptic inhibition in both GCs and SGCs in slices, mediate sustained feedback inhibition selectively in SGCs. The temporally selective blunting of activity-driven sustained inhibitory gating of SGCs could support their preferential and persistent recruitment during behavioral tasks.

Keywords: parvalbumin, dentate gyrus, GABA, feedback inhibition

Introduction:

The hippocampal dentate gyrus is a circuit known for its sparse activity, a unique feature essential for its function as a site of pattern separation, a process of disambiguating similar inputs into distinct patterns of neural activity and memory representations (Bekinschtein et al., 2013; GoodSmith et al., 2017). The characteristically low levels of dentate activity are maintained by the relatively hyperpolarized resting membrane potential and low input resistance of the projection neurons and their powerful inhibitory regulation (Heinemann et al., 1992; Lothman et al., 1992). Dentate inhibition includes sustained tonic/extrasynaptic GABA currents as well as distinct phases of synaptic inhibition, which shape both basal and afferent-evoked activity (Ewell and Jones, 2010; Larimer and Strowbridge, 2010; Stell et al., 2003). Apart from the classical basal spontaneous synaptic inhibition and afferent evoked feedforward and feedback inhibition, dentate granule cells (GCs) have been proposed to receive "sustained" increase in feedback synaptic inhibition following paired stimulation of perforant path (PP) inputs (Larimer and Strowbridge, 2010). This sustained feedback inhibition has been suggested as a mechanism for surround inhibition needed to facilitate pattern separation (Larimer and Strowbridge, 2010; Walker et al., 2010). However, the reliability, cell-specificity and temporal structure of this sustained feedback inhibition is not known and the identity of inhibitory neurons recruited during this prolonged feedback inhibition has not been examined.

Although dentate GCs have, for long, been considered a structurally and functionally uniform class of projection neurons, detailed morphometric and physiological analysis in rats have revealed a sparse, structurally distinct population of projection neurons described as semilunar granule cells (SGCs) by Ramón y Cajal (1995) (Gupta et al., 2012; Gupta et al., 2020; Save et al., 2018; Williams et al., 2007). Functionally, SGCs have sustained firing in response to

afferent stimulation, which distinguish them from GCs (Larimer and Strowbridge, 2010). While SGCs, characterized by wider dendritic span, have been reported in mice (Erwin et al., 2020; Rovira-Esteban et al., 2020; Save *et al.*, 2018), detailed morphometric analysis and functional characterization of murine SGCs is lacking. Of particular relevance to dentate inhibitory regulation, whether SGCs receive similar early (feedforward or disynaptic feedback) as well as sustained polysynaptic feedback inhibition as GCs or may escape this inhibitory gate is currently unknown. Studies in adolescent rats show that SGCs have higher tonic GABA currents and receive more frequent synaptic inhibitory inputs than GCs (Gupta *et al.*, 2012; Gupta *et al.*, 2020). Uniquely, SGCs show reduction in both tonic GABA currents and frequency of synaptic inhibitory inputs after brain injury rather than the increase observed in GCs (Gupta *et al.*, 2012). While these findings suggest different interneuron subtypes may contribute to synaptic inhibition in GCs and SGCs, which class of dentate interneurons underlie this differential control, is not known. Parvalbumin-interneurons (PV-INs) are a major class of GABAergic neurons which are classified by expression of the calcium binding protein parvalbumin and their fast, non-adapting firing pattern. PV-INs include the perisomatically projecting basket cells which contribute to feedforward and feedback inhibition of GCs (Ewell and Jones, 2010; Hefft and Jonas, 2005; Kraushaar and Jonas, 2000) and axo-axonic cells which target granule cell axon-initial segments (Howard et al., 2005; Sik et al., 1997). A single basket cell can project to as many as 10,000 GCs (Freund and Buzsaki, 1996; Santhakumar, 2008) and is an ideal candidate to mediate surround inhibition. However, whether PV-INs innervate SGCs with somata located in the inner molecular layer, outside the dense axon collaterals of parvalbumin positive basket cells has not been tested.

Recent studies have indicated that SGCs may be disproportionately recruited to memory engrams (Erwin *et al.*, 2020) making it important to understand whether inhibitory regulation of SGCs

differs from that of GCs. This study was conducted to systematically examine the cell-type specific differences in distinct phases of synaptic inhibition; basal spontaneous synaptic inhibition, PP evoked, early feedforward, and feedback inhibition as well as sustained feedback inhibition, between the two classes of dentate projection neurons and to determine the contribution of PV-INs to specific phases of inhibition in GCs and SGCs.

Results

Quantitative morphometry resolves murine GCs and SGCs into distinct groups.

Recordings were obtained from neurons in the inner molecular layer (IML) and granule cell layer followed by *post hoc* recovery of cell morphologies from biocytin fills (Fig. 1, Fig. S1). Unsupervised clustering of morphometric data obtained from reconstruction of neurons in which dendritic arbors were fully recovered was used to verify whether the somato-dendritic parameters distinguishing GCs from SGCs in mice are similar to those characterized in rats (Gupta *et al.*, 2020; Williams *et al.*, 2007). Projection neurons were identified based on the presence of spiny dendrites in the molecular layer and axons with mossy fiber boutons entering the hilus and targeting CA3 (Gupta *et al.*, 2020). Morphometric parameters of the cells reconstructed in 3D were obtained using automated algorithms in Neurolucida Explorer (Tables S1-2, adapted from Gupta *et al.*, 2020). Principal Component Analysis (PCA) of 42 morphometric parameters from 17 cells revealed that the first two principal components (PCs) explained more than 50% of the total variance in the data, while the first seven components explained 90% of the variance (Fig S2A). Hierarchical cluster analysis on PCs (HCPC) on the first seven PCs suggested partitioning of cells into three clusters (Fig. S2B) as illustrated on the factor map produced by the first seven PCs (Fig S2C). In spite of the exclusion of categorical variables such as soma location from HCPC, cells classified as GCs and SGCs by investigator (M.A) segregated into two distinct clusters based on Dim1. Interestingly, cells classified as GCs further segregated into two clusters (Clusters #1 and #2) based on Dim2. Variables more than 70% correlated with the 1st PC were identified as most responsible for PC formation. Evaluation of the quantitative variables underlying the clusters revealed that cluster #3, comprised of putative SGCs, was distinguished by a higher number of primary dendrites, greater dendritic angle, soma width, and cell surface

area and lower dendritic complexity (Fig. 1, Fig. S2). While cells in Cluster #1 had fewer, typically one, primary dendrite, lower dendritic angle and higher dendritic complexity, Cluster #2 segregated based on the presence of more fourth order segments, ends and intersections (Fig. S2). Interestingly, dendritic angle was different between groups, increasing from Cluster #1 to Cluster #3 (Fig. S2D). The number of primary dendrites in Cluster #3 (putative SGCs) was significantly higher than in both Clusters #1 and #2 (Fig. S2E). Similarly, Cluster #3 (putative SGCs) had the least dendritic complexity which was significantly lower than in Cluster #1 while differences in dendritic complexity between Clusters #1 and #2 failed to reach statistical significance (Fig. S2F).

Morphometric parameters from putative GCs (Clusters #1 and #2) were pooled together and compared with Cluster #3 (putative SGCs) for further analysis. Similar to findings in rats (Gupta *et al.*, 2020), GCs and SGCs differed in dendritic angle, number of primary dendrites, soma aspect ratio and dendritic complexity (Fig. 1, Table S3,4). In contrast, certain global parameters such as total number of dendritic ends and total length of dendrites were not different between the cell types (Fig. 1). Like GCs, SGC axons extended to CA3 and showed mossy fiber terminals in the hilus (Fig. 1A-B). Together these data provide the first comprehensive morphometric comparison of GCs and SGCs in mice and demonstrate that the presence of 3 or more primary dendrites and wide dendritic angle reliably distinguishes SGCs from GCs.

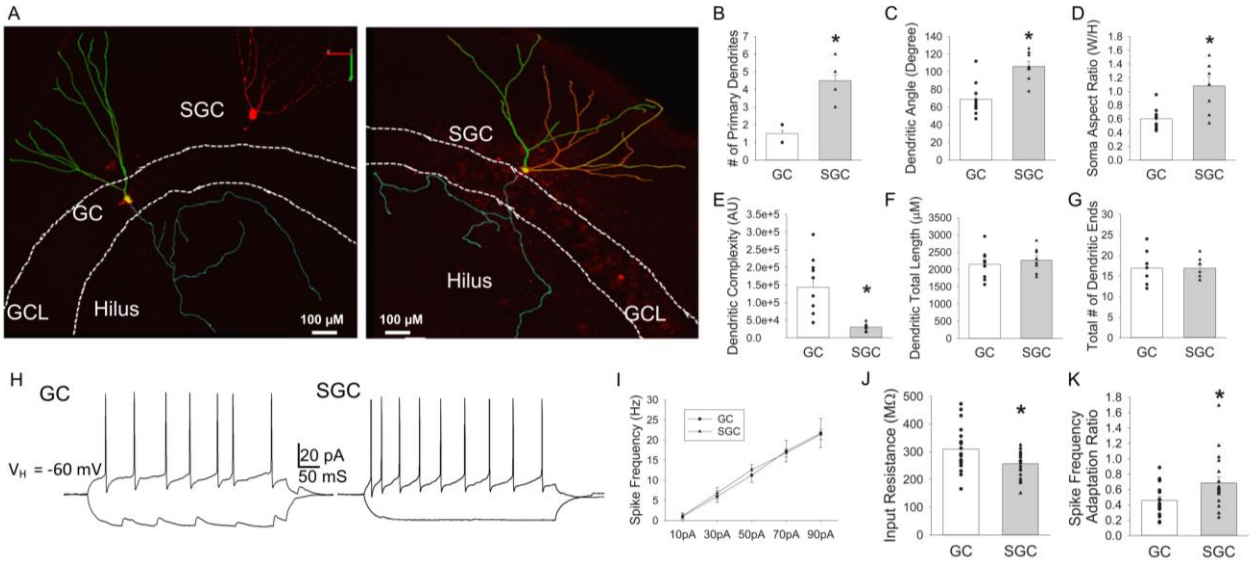

Figure 1. Morphological and physiological characteristics of murine GCs and SGCs. A. Overlay of confocal image and Neurolucida 360 reconstruction of a biocytin filled GC (left) and SGC (right) show dendritic arbors and axon projection towards CA3. Cyan: axons; Orange, Green, Yellow: dendritic trees. B-G. Summary plots of morphological parameters including number of primary dendrites (B), dendritic angle (C), soma aspect ratio (D), dendritic complexity (E), dendritic total length (F) and total number of dendritic ends (G) between GCs (n=10) and SGCs (n=8). H. Voltage traces in response to +70 pA and -100 pA current injections in a GC (left) and SGC (right) illustrate firing pattern and passive properties. I. Summary plot of firing frequency in response to increasing current injections in GCs (n=8) and SGCs (n=10). J-K. Summary histogram of input resistance (measured from response to -100 pA), (J) and spike frequency adaptation ratio (K) in GCs (n=18) and SGCs (n=19). Data presented as mean±sem. * indicates $p<0.05$ by independent t-test.

SGCs differ from GCs in intrinsic physiology and frequency of basal synaptic inhibition.

Examination of active and passive responses to graded current injections revealed no difference in firing frequency between the two cell types (Fig. 1 H-I). However, input resistance was significantly lower in SGCs (Fig. 1J). Spike frequency adaptation ratio (ratio of inter-spike interval between first 2 and last 2 spikes during a +70 pA current injection) in SGCs was lower than in GCs (Fig. 1K). These findings are consistent with differences in intrinsic properties identified between the SGCs and GCs (Erwin *et al.*, 2020; Gupta *et al.*, 2012; Save *et al.*, 2018; Williams *et al.*, 2007).

Spontaneous inhibitory postsynaptic currents (sIPSCs), recorded from holding potential of -60 mV in the presence of glutamate blockers, were more frequent in SGCs (Fig. 2: sIPSC frequency in Hz, GCs: 8.38±1.14, N=18, SGCs: 13.48±1.07, N=19, $p<0.05$, t-test). However, sIPSCs amplitude (Fig. 2D: sIPSC amplitude in pA, GCs: 42.98±3.35, N=18, SGCs: 41.52±3.01, N=19, $p>0.05$, t-test), amplitude weighted decay time constant ($\tau_{decay\text{-}WT}$) and 20-80% rise times were not different between GCs and SGCs (Fig. 2E-F). These findings demonstrate that murine SGCs show the same structural and functional distinctions from GCs identified in prior studies in rats (Gupta *et al.*, 2012; Gupta *et al.*, 2020). These data validate the morphological criteria which we used distinguish to GCs and SGCs in the subsequent experiments and indicate differences in inhibitory inputs between the cell types.

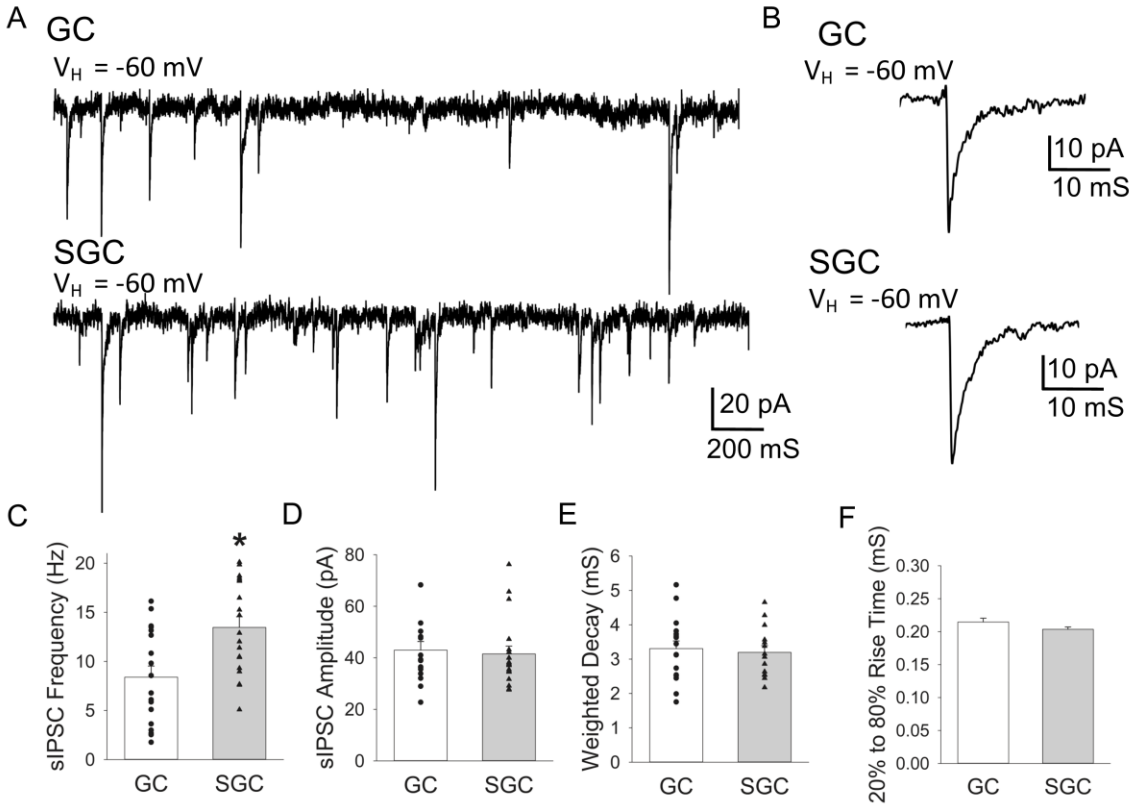

Figure 2. SGCs receive more spontaneous inhibitory synaptic events than GCs. A. Representative current traces from a holding potential of -60 mV illustrate sIPSCs in a GC (above) and SGC (below). B. Example of average sIPSC trace from a GC (above) and SGC (below). C-F. Summary histogram of sIPSC frequency (C), amplitude (D), amplitude weighted decay time constant (E) and 20-80% rise time (F) in GCs (n=18) and SGCs (n=19). Data presented as mean±sem. * indicates $p<0.05$ by independent t-test.

Limited role of parvalbumin interneurons in steady-state synaptic inhibition of GCs and SGCs in slices.

To determine whether differential inputs from parvalbumin expressing interneurons (PV-INs), contribute to the higher action potential-dependent sIPSCs frequency in SGCs we examined if optical suppression of PV-INs in mice expressing the inhibitory opsin, halorhodropsin (NpHR3), under control of the PV promotor reduced sIPSC frequency. Validity of the PV-cre mouse line was confirmed by colocalization of parvalbumin and YFP using immunostaining (not shown) and by fast, non-adapting firing in recordings from YFP positive neurons (Suppl. Fig. 3A, Fig. 6A). Since activation of NpHR3 can reduce the chloride gradient (Alfonsa et al., 2015), light exposure was restricted to 2s periods. Recordings from YFP labeled neurons established that the 2s amber light illumination reliably and reversibly hyperpolarized YFP positive fast spiking neurons (Fig. 3B, n>10 cells) and suppressed action potential firing (Suppl. Fig. 3A, Fig. S3, SI. Fig. 5A-D). Spontaneous IPSCs were recorded from GCs and SGCs for a total of seven minutes, with a two-minute baseline followed by five one-minute cycles with a 2s exposure to amber light at the beginning of each cycle followed by time for recovery of the chloride gradient between light exposure (Fig. 2A). Spontaneous IPSC parameters measured during the 2s prior to light exposure were averaged and compared to the parameters averaged over the periods during the five cycles of light exposure. Contrary to expectations, optical suppression of PV-INs failed to reduce both frequency and amplitude of GC sIPSCs (Fig. 3 C-E, n=5 cells, p>0.05, paired t-test). Similarly, optical suppression of PV-IN firing failed to reduce sIPSC frequency in SGCs as well (Fig. 3 C-E, n=5 cells each, p>0.05, paired t-test). These data raise a surprising possibility that PV-INs may not contribute to basal sIPSCs in either GCs or SGCs in acute slice preparations.

Given the unexpected outcome, and since the optogenetic system was functionally validated (Fig. 3B, Fig. S3A), we considered whether use of glutamate receptor antagonist to isolate IPSCs may have reduced PV-IN firing and underestimated their contribution to sIPSCs. To address this possibility, IPSCs were recorded as outward currents from cells held at 0 mV (reversal for glutamatergic currents) using a low chloride internal. As expected, sIPSC frequency recorded in the absence of glutamate blockers was higher (Fig 3G-H) than that recorded in glutamate receptor blockers (Fig 2 and 3C-D) in both cell types. Nevertheless, sIPSC frequency and amplitude in GCs were not reduced by amber light suppression of PV-INs (Fig. 3F-H: frequency in Hz, no-light: 26.80±3.78, light: 28.32±2.41; amplitude in pA, no-light: 26.43±2.88, light: 25.46±2.10, N=13, $p>0.05$, paired t-test). Similarly, sIPSC parameters in SGCs were also unaltered during amber light exposure (Fig. 3F-H: frequency in Hz, no-light: 35.77±5.44, light: 36.81±4.48; amplitude in pA, no-light: 28.96±3.72, light: 26.74±3.17, N=11, $p>0.05$, paired t-test). Together, these data obtained under two different recording conditions support the surprising conclusion that PV-INs contribute minimally to basal sIPSC frequency in both dentate projection neuron subtypes.

While unlikely, a potential reason for the above outcome is that a majority of the sIPSCs in our recordings were action potential independent miniature events, which would not be modified by suppressing PV-IN firing. To exclude this possibility, we tested the ability of the sodium channel antagonist tetrodotoxin (TTX, 1μM) to reduce frequency of IPSCs indicating the presence of action potential driven events. As expected, TTX significantly reduced IPSC frequency in both GCs (Fig. S4 C, E-G, 88.42 % reduction, N=7, $p<0.05$, paired t-test) and SGCs (Fig. S4 D, E-G, 83.36% reduction, $p<0.05$, paired t-test). TTX also reduced IPSC amplitude in both cell types (not shown). Overall, the ability of TTX to suppress >80% of events indicates that majority of

sIPSCs in both SGCs and GCs are driven by interneuron firing. Taken together, these data support the conclusion that PV-INs do not contribute significantly to action potential driven basal sIPSCs in both GCs and SGCs in slice preparations.

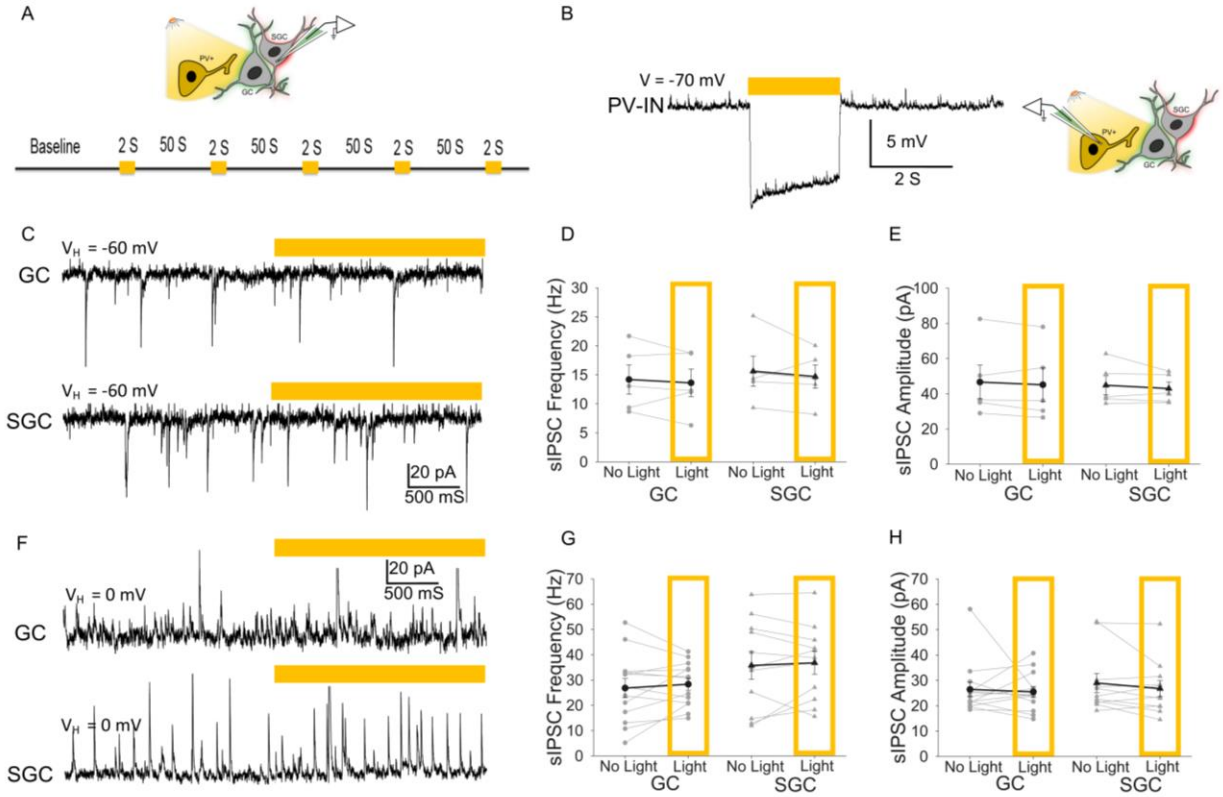

Figure 3. Optical suppression of PV-INs fails to reduce sIPSC frequency in both GCs and SGCs. A) Schematic of the experimental paradigm illustrates amber light stimulation of NpHR3-YFP expressing PV-IN while recording from GC/SGC (above) and the protocol for light OFF and light ON condition below. B. Membrane voltage trace from an NpHR3-YFP expressing PV-IN shows rapid and reversible hyperpolarization during the 2s amber light stimulation. C. Current traces from a GC (above) and SGC (below) recorded from a holding potential of -60 mV using high-chloride internal shows sIPSCs as inward currents before and during NpHR3 activation (amber bar) in PV-INs. IPSCs were isolated in kynurenic acid (3 mM). D-E. Plots summarize effect of optical suppression of PV-IN on sIPSC frequency (D) and amplitude (E) (n=5 GCs and SGC). F. Representative traces illustrate sIPSCs in a GC (above) and SGC (below) before and during activation amber light exposure (amber bar). Recordings were obtained using a low-chloride internal from a holding potential of 0 mV without synaptic blockers. G-H. Summary plots of effect amber light on sIPSC frequency (G) and amplitude (H) in GCs (n=13) and SGCs (n=11). Data presented as mean±sem.

Activation of parvalbumin interneurons drives synaptic inhibition in both GCs and SGC.

Since sIPSCs represent synaptic inhibition in the absence of afferent inputs, we examined whether direct optical activation of PV-IN evoked IPSCs (oeIPSCs) in GCs and SGCs in slices from mice expressing channelrhodopsin (ChR2) in PV-INs. Following baseline recordings of sIPSCs in glutamate antagonist without light, recordings were continued during optical activation of ChR2 in PV-IN using blue light (λ=473nm, 10 s). Optical activation of PV-INs elicited a significant increase in IPSC frequency in GCs (Fig. 4; frequency in Hz, no-light: 8.45±1.31, light: 52.11±5.92, N=14, $p<0.05$, paired t-test) confirming the robust PV-IN input to GCs. PV-IN activation increased IPSC frequency in SGCs as well (Fig. 4A-C: frequency in Hz, no-light: 13.68±1.20, light: 59.49±4.62, N=14, $p<0.05$, paired t-test), demonstrating functional PV-IN innervation of SGCs. However, IPSC peak amplitude was not increased by optical activation of PV-INs in either GCs or SGCs (Fig. 4). Interestingly, while the IPSC frequency during blue light exposure was not different between GCs and SGCs, PV-IN induced increase in IPSCs frequency was greater in GCs than in SGCs (Fig. 4D: % increase in sIPSC frequency, GCs: 719.12±141.61, SGCs: 355.58±40.16, N=14, $p<0.05$, independent t-test). These data demonstrate that SGCs, like GCs, receive PV-IN inputs and that direct activation of PV-INs leads to a greater increase synaptic inhibitory events in GCs. Since PV-INs are known to be recruited during PP activation and support feedforward and feedback GC inhibition (Ewell and Jones, 2010), we examined whether recruitment of inhibition by afferent stimulation differed between the cell types. PP stimulation at increasing intensities evoked IPSCs in both SGCs and GCs. The peak amplitude of afferent evoked IPSCs was not different between cell types (Fig. 4E-G), demonstrating that both GCs and SGCs receive similar early feedforward/feedback inhibition upon PP stimulation.

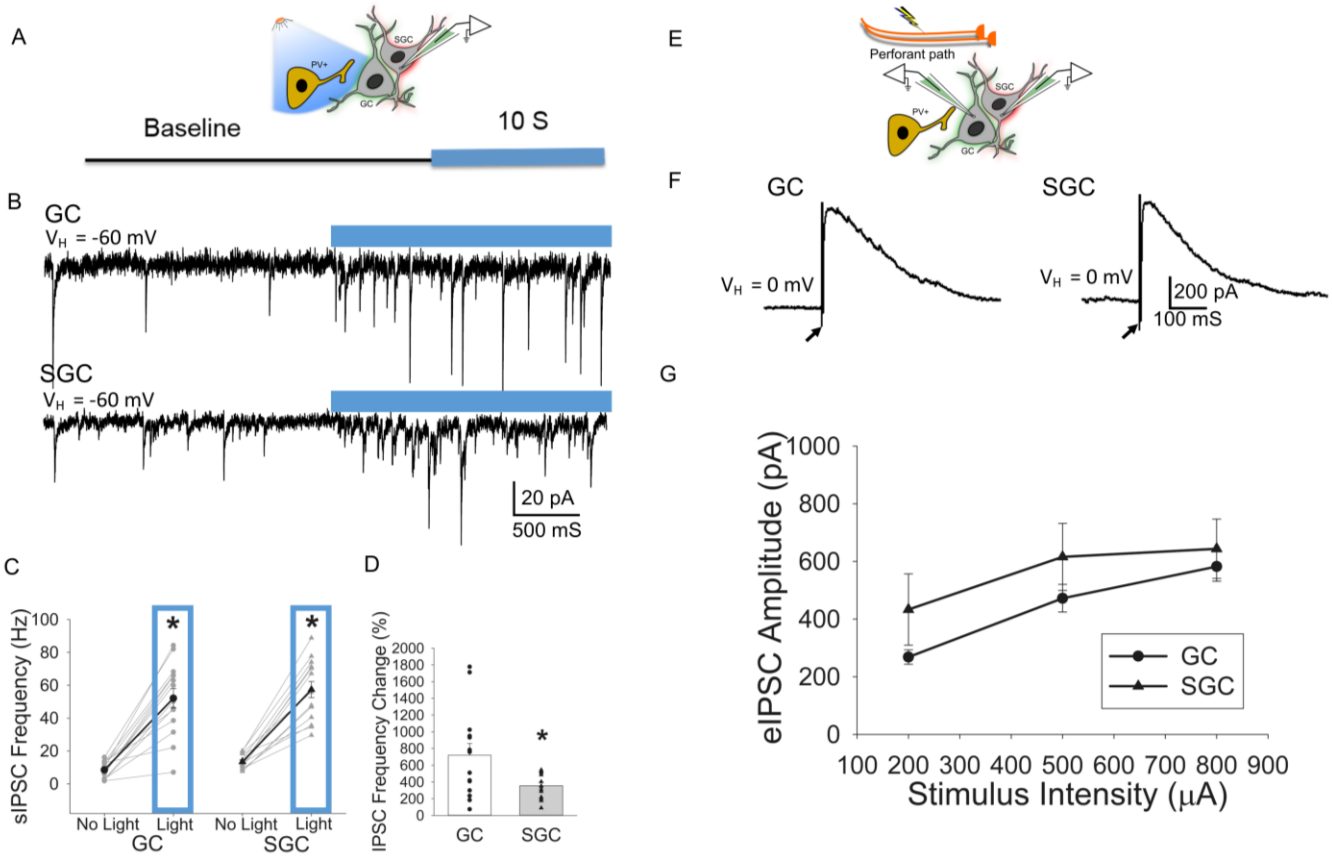

Figure 4. Activation of PV-INs and afferent stimulation evoke inhibitory synaptic currents in both dentate projection neuron subtypes. A. Schematic illustrates blue light stimulation of ChR2-YFP expressing PV-IN while recording from GC/SGC (above) and light OFF and light ON protocol below. B) Example recordings from a GC (above) and SGC (below) illustrate sIPSCs before and during optical activation of PV-INs. Cells were held at -60 mV and kynurenic acid (3 mM)was used to isolate IPSCs. C. Summary plots of sIPSC frequency before and during blue light exposure in GCs (n=14) and SGCs (n=14). D. Plot of percent change in IPSC frequency during optogenetic activation of PV-IN. E. Schematic of the experimental paradigm illustrates PP stimulation while recording from GC/SGC. F. Perforant path evoked IPSC in GC and SGC recorded as outward currents using a low-chloride internal and a holding potential of 0 mV. G. Summary plot of eIPSC peak amplitude in GCs and SGCs in response to stimulation of the PP at increasing current intensities. Data presented as mean±sem. * indicates $p<0.05$ by paired (panel C) or unpaired (panel D) t-test.

Afferent stimulation drives greater enhancement of sustained feedback inhibition in granule cells.

A functional characteristic of SGCs, not observed in GCs, is their unique ability for sustained firing in response to paired afferent stimuli in rat hippocampal slices, which has been proposed to drive feedback inhibition and sculpt pattern separation (Larimer and Strowbridge, 2010). We examined the reliability and reproducibility of SGC sustained firing in murine SGCs. As is typical for GCs, a single PP stimulus evoked a single action potential in GCs (3/3 cells tested) as well as in SGCs (4/4 cells tested) but failed to elicit sustained spiking. However, when the PP was stimulated with a pair of suprathreshold stimuli at 10 ms interval, consistent with theta frequency inputs (Braganza et al., 2020; Larimer and Strowbridge, 2010), a subset of SGCs showed prolonged spiking activity. Sustained firing was observed in 51.51% of the trials (Fig 5 A-B, 17/33 of trials in 2/4 SGCs). The sustained firing was initiated between 200 ms to 2s after the paired stimulation, although the latency to sustained firing was over 6s in a few trials (Fig. 5C, median 1.14s IQR: 0.61-1.9s). This evoked sustained firing in SGC lasted several seconds, at times until the end of the recording 20s after stimulation (Fig. 5D). On average, the sustained firing lasted 15s, which is likely an underestimate due to the termination of recordings. None of the GCs tested exhibited firing beyond the early evoked firing in any of the trials (0/12 trials, 3 GCs).

Sustained firing in SGCs has been correlated with hilar mossy cell and interneuron firing as well as reduced GC excitability (Larimer and Strowbridge, 2010). However, whether GCs receive enhanced synaptic inhibition during this period and whether SGCs undergo a parallel sustained increase in feedback synaptic inhibition is not known. Using simultaneous recordings in GC-SGC pairs (Fig 5E), we directly compared recruitment of polysynaptic sustained inhibition in GCs and SGCs following paired PP stimulation. Paired PP stimuli elicited a large early eIPSC

peak (Fig. 5 E1 insets) followed by a prolonged barrage of "evoked-sustained" IPSCs (esIPSCs) lasting over 20s in both GCs and SGCs (Fig. 5E1). To better characterize the evoked sustained activity, we binned IPSCs into 5s segments before the stimulus and 1s segments 500ms-10.5s after the stimulation, with additional 5s segments 15-20s and 25-30s post-stimulus. The 500 ms delay for stimulation was adopted to avoid the maximum conductance during eIPSC, which tended obscure individual events. Although the sIPSC frequency in the pre-stimulus period was stable within each cell, it varied considerably between cells. To normalize for the variability, the difference in IPSC frequency following stimulation was normalized to the pre-stimulus sIPSC frequency averaged over 3 X 5-sec pre-stimulus bins ((post-pre)/pre*100). Both GCs and SGCs showed a significant post-stimulus increase in esIPSC frequency lasting over 20s. In addition to the significant effect of time, the difference between cell types was statistically significant (Fig. 5F, $F_{(1,11)}=9.4$, for effect of time and $F_{(1,11)}=4.9$ for cell-type, $p<0.05$ by Two-way RM ANOVA). Pairwise comparison between cell types, revealed that the increase in esIPSC frequency normalized to pre-stimulus frequency was significantly greater in GCs than in SGCs. Both GCs and SGCs showed increase in esIPSC frequency for up to 10s post stimulus reaching similar maximum frequency and declining back to pre-stimulus levels by 20-30s. However, the increase in esIPSC frequency (normalized to pre-stimulus frequency) quantified over the first 500-1500ms (1s) after stimulation was significantly higher in GCs than in SGCs ($p<0.05$, by TW-RM ANOVA followed by Pairwise Multiple Comparison using Holm-Sidak method).

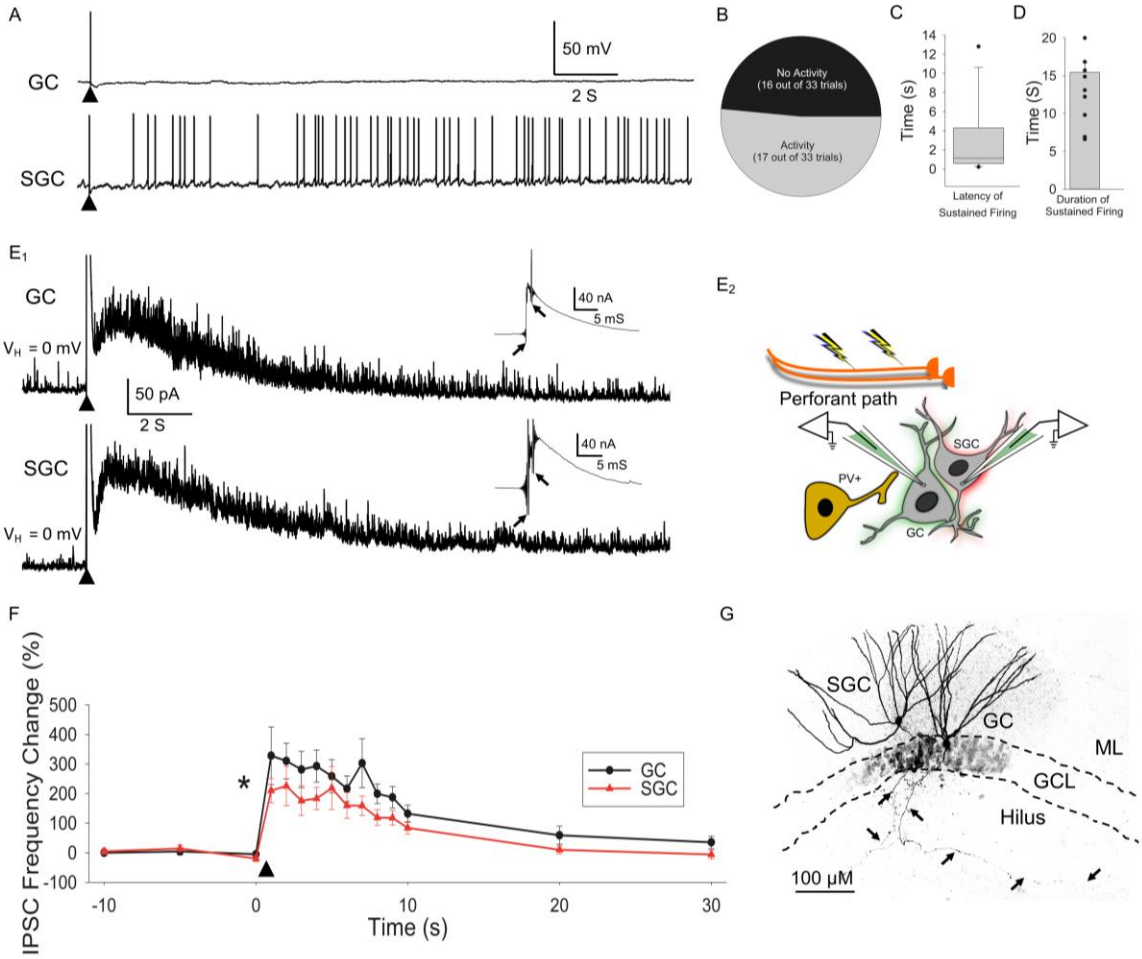

Figure 5. Afferent evoked prolonged SGC firing is associated with sustained increase in sIPSC frequency in both GC and SGC. A. Membrane voltage traces in a GC (above) and SGC (below) evoked by a pair of suprathreshold stimuli to the PP. Note prolonged firing in the SGC while none of the GCs (n=3 cells, 12 trails) showed more than 1-3 spikes. B. Plot shows the proportion of trials that evoked sustained firing in SGCs (n= 4 cells, 33 trials). C-D. Plots illustrate the distribution of latency from afferent stimulation to the start of sustained firing (C) and duration of sustained firing in SGCs recorded for a maximum of 20s after stimulation. E. Schematic of paired GC-SGC recordings in response to paired PP stimulation (E_2). Current traces of simultaneously recorded GC-SGC pair illustrate the sustained increase in IPSC frequency compared to pre-stimulus baseline (E_1). The eIPSC peak is truncated to better illustrate the sustained change in IPSCs over 20s. Insets: traces at a different scale illustrate the peak eIPSC amplitude. F. Summary plot of sIPSC frequency in GCs and SGCs (n= 12 each) prior to stimulation (binned over 5s) and evoked sustained IPSC frequency (1s bins for the first 10s and 5sec bins at 20 and 30s) for success rate in induction of prolonged spiking activity in GCs (12 trials, N=3) and SGCs (33 trials, N=5). G. Maximum intensity projection of a confocal image stack of a GC-SGC pair filled during recordings (presented as grey scale and inverted) illustrate dendric arbors and hilar axon (arrows). GCL: granule cell layer; ML: molecular layer, GC: granule cell; SGC: semilunar granule cell. Data presented as median(interquartile range for in C and mean±sem in D and F. * indicates $p<0.05$ for effect of cell-type ($F_{(1,11)}=4.9$) by TW-RM ANOVA.

Interestingly, not all cells showed robust esIPSC barrages even within the same slice, suggesting cell specific recruitment of feedback inhibition. We found that 16.67% (2/12) GCs and 33.33% (4/12) SGCs failed to show esIPSC barrage, defined as doubling in basal frequency in the first 3 post-stimulus bins examined (3s). Additional recordings conducted in the presence of the $GABA_A$ receptor antagonist, gabazine (10 µM) confirmed that, like eIPSC, esIPSCs were also eliminated by gabazine (Fig. S4). These results demonstrate that paired PP stimulation results in prolonged changes to dentate inhibition and SGC excitability. Crucially, the data reveal that the relative increase in sustained feedback inhibition in SGCs is less than in GCs and suggest that in spite of their higher basal inhibitory tone and glutamatergic drive (Larimer and Strowbridge, 2010) SGC show lower increase in inhibitory gating than GCs following activation of inputs.

Role of PV-INs in sustained feedback inhibition of dentate projection neurons following paired afferent stimulation.

Since PV-INs are known to mediate strong granule cell feedforward and feedback inhibition (Hefft et al., 2002), we examined whether they exhibit sustained firing in response to paired PP stimuli coinciding with increased esIPSCs in GCs. PV-INs in the hilar granule cell border were identified based on YFP labeling and confirmed by the high frequency, non-adapting firing (Fig. 6A, insets). PV-IN voltage traces in responses to paired PP stimulation (Fig. 6A) are illustrated alongside the time course of esIPSC in a GC (Fig. 6D) for reference. Interestingly, only 54.5% (6/11 cells) PV-INs showed sustained increase in firing upon paired PP stimulation. An additional 18.2% (2/11 cells) PV-INs received increased EPSC drive during this period suggesting that they may be driven by SGC firing (Fig. 6B). However, 27.3% (3/11) PV-INs showed no apparent sustained change in EPSC frequency upon PP stimulation in spite of the early evoked firing. The prolonged PV-IN firing followed the initial stimulation with a median

latency of 1.02s (IQR 0.62-2.03s) which was similar to the latency to evoked SGC firing (Fig. 6C) and consistent with the timeline of the esIPSC in GC/SGCs. These data suggest that the sustained firing in SGCs likely drives PV-IN firing and raise the possibility that PV-INs contribute to a certain component of esIPSCs in dentate projection neurons.

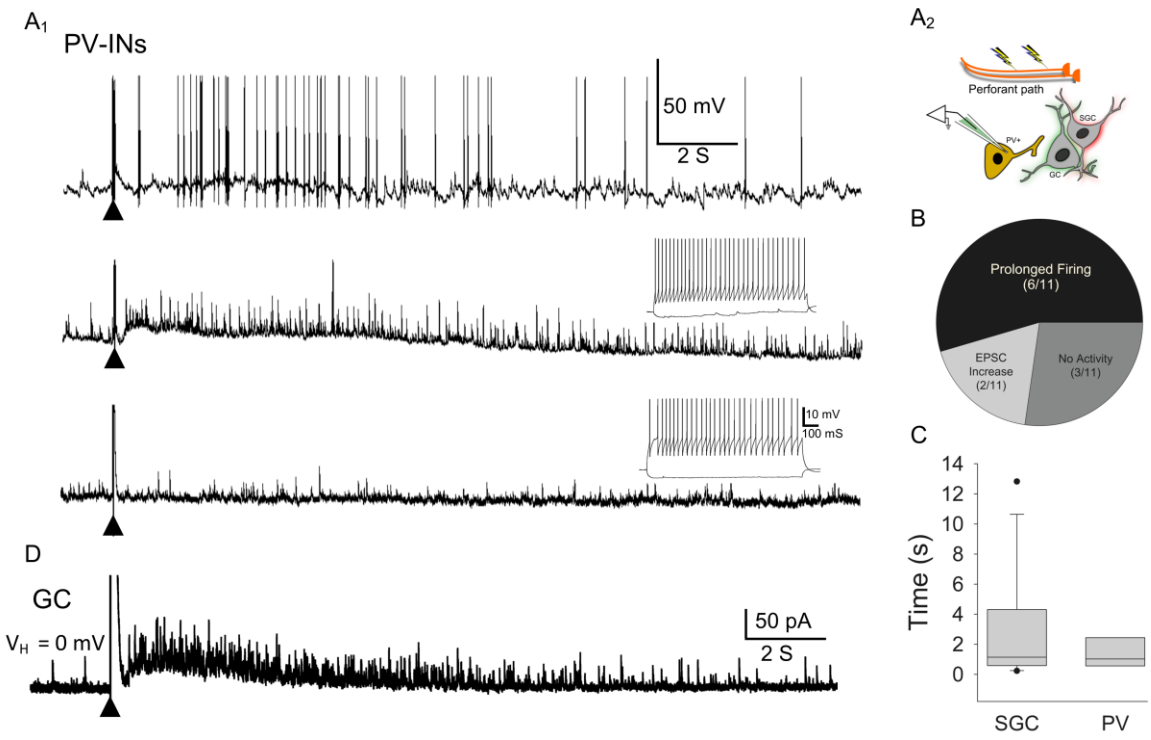

Figure 6. Increase in PV-IN excitability during evoked sustained sIPSCs in dentate projection neurons. A. Example traces show increased firing (above), enhanced EPSP barrages (middle) and unaltered EPSP frequency (below) in YFP-positive PV-INs (A_1) in response to the paired PP stimulation paradigm illustrated in A_2. Insets in middle and lower traces illustrate high frequency firing in recorded PV-IN. B. Pie chart summarizes the proportion of PV-INs that showed evoked sustained firing, EPSP increase or no change in response to stimulation (n= 11 cells, 33 trials). C. Plot illustrates the distribution of latency of enhanced PV-IN firing following paired PP stimulation. D. Current traces from a GC showing sustained IPSCs is included for comparison.

To verify whether halorhodopsin suppression could reduce PP-evoked PV-IN firing, we performed control recordings from YFP-labeled neurons in PV-NpHR3 mice. While optical suppression failed to fully eliminate firing of PV-INs in response to paired PP stimulation it consistently reduced firing without altering firing in hilar interneurons and putative mossy cells lacking YFP expression (Fig. S5). Additionally, we verified that optical suppression of PV-INs did not induce persistent firing in GC or eliminate sustained firing in SGCs (Fig. S5).

To directly test the contribution of PV-INs to esIPSC barrages in GCs and SGCs, we recorded esIPSCs in putative GC/SGC pairs in PV-NpHR3 mice in the absence or presence of amber light (2s exposure starting 100ms after the onset of PP stimulation). Light-on and light-off conditions randomized (Fig. 7, trials with red lined in Fig. 7D indicate light-on first recordings). Surprisingly, esIPSC frequency, normalized to basal sIPSC frequency prior to stimulation, was not reduced by optical suppression of PV-INs (Fig. 7D: esIPSC frequency as % of pre-stimulus frequency, no-light: 264.59±49.76, light: 225.85±43.08, N=8, $p>0.05$, by paired t-test). In contrast, recordings from SGCs showed a significant reduction in esIPSC frequency during suppression of PV-INs with amber-light (Fig. 7D: esIPSC frequency as % of pre-stimulus frequency, no-light: 209.76±57.92, light: 127.86±41.15, N=8, $p> 0.05$ by paired t-test). Thus, optical suppression of PV-INs selectively reduced esIPSC frequency in SGCs to approximately half of that observed in the absence of light demonstrating fundamental differences in inhibitory regulation of GCs and SGCs during evoked activity.

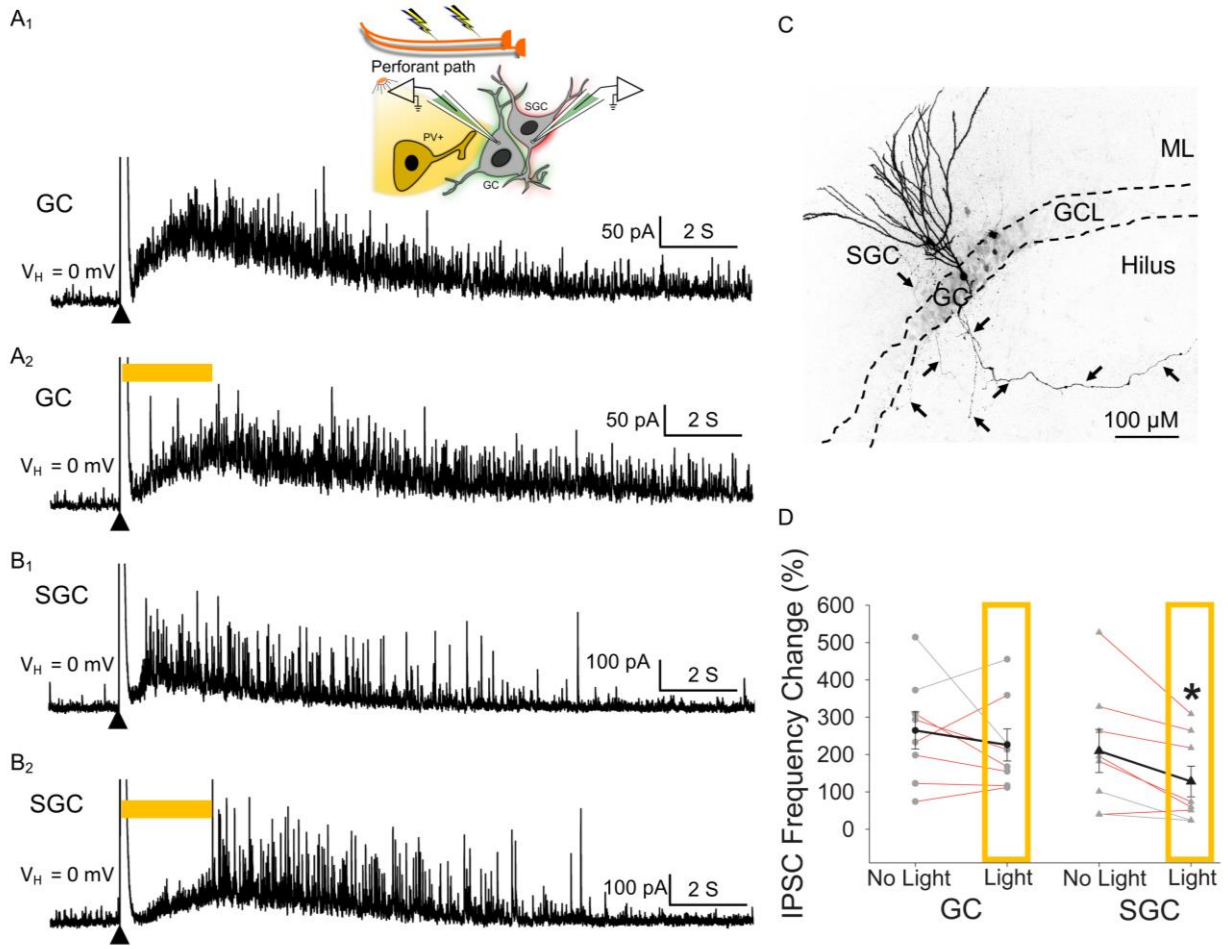

Figure 7. Optical suppression of PV-INs selectively reduces evoked sustained IPSCs in SGCs. A_1. Schematic illustrating the simultaneous dual GC-SGC recordings in response to paired stimulation of the PP and amber light stimulation (above). GC current trace illustrates the sustained increase in IPSC frequency compared to pre-stimulus baseline (below). A_2. GC trace shows that evoked sustained IPSCs in response to paired afferent stimuli appears unchanged by amber light suppression (amber bar) of PV-INs. B_1. SGC current trace illustrates the sustained increase in IPSC frequency compared to pre-stimulus baseline. B_2. SGC trace shows that evoked sustained IPSCs in response to paired afferent stimuli are suppressed by amber light. Note that the eIPSC peak is truncated to better illustrate the sustained change in IPSCs over 20s. C. Maximum intensity projection of a confocal image stack of a GC-SGC pair filled during recordings illustrated the soma location dendric arbors and hilar axon (arrows) of the cells. The image is presented as grey scale and inverted to better illustrate the axon. GCL: granule cell layer; ML: molecular layer, GC: granule cell; SGC: semilunar granule cell. D. Summary plots of effect of amber light suppression of PV-INs on evoked sustained IPSC frequency in GCs and SGCs (n=8 each). Red lines indicate trials with light-on first recordings. Data presented as mean±sem. * indicates $p<0.05$ by paired t-test.

Discussion:

This study distinguishes three distinct phases of synaptic inhibition in dentate projection neurons and identifies that lateral sustained feedback inhibition which has been proposed to shape dentate pattern separation and memory engram formation is significantly lower in SGCs, a subclass of dentate projection neurons. Specifically, our study reveals cell-type specific differences in the role for parvalbumin interneurons which support activity-driven sustained lateral inhibition of SGCs, but not GCs. These findings suggest SGCs differ from GCs in local circuit feedback inhibitory regulation during afferent activation, which could shape their distinct role in dentate processing.

SGCs, originally defined by Ramón y Cajal (1995) are a sparse, developmentally and functionally distinct subpopulation of dentate output neurons (Gupta *et al.*, 2012; Gupta *et al.*, 2020; Larimer and Strowbridge, 2010; Save *et al.*, 2018; Williams *et al.*, 2007). Inhibitory regulation is central to dentate information processing and helps maintain the sparse granule cell activity needed for pattern separation (Arima-Yoshida et al., 2011; Dengler and Coulter, 2016; Hainmueller and Bartos, 2020). Dentate inhibition is diverse in its spatial and temporal structure and is supported by multiple classes of interneurons targeting distinct somato-dendritic compartments of the projection neurons. Temporally, in addition to the steady-state spontaneous synaptic inhibition and afferent evoked mono- and disynaptic feedforward and feedback inhibition, granule cells have strong extrasynaptic inhibition (Kraushaar and Jonas, 2000; Soltesz et al., 1995; Stell *et al.*, 2003). Additionally, afferent stimulation has been proposed to recruit sustained polysynaptic feedback inhibition in GCs (Larimer and Strowbridge, 2010). While we previously reported that SGCs have greater steady-state tonic and synaptic GABA currents (Gupta *et al.*, 2012; Gupta *et al.*, 2020), whether feedback inhibitory regulation of SGCs differs

from GCs during input activation and the temporal profile and reliability of the feedback inhibition were not known. We demonstrate three functionally distinct phases of synaptic inhibition, namely, basal, early evoked, and sustained feedback synaptic inhibition in both GCs and SGCs. Our data provide the first characterization of the temporal profile and reliability of dentate evoked-sustained inhibition and demonstrates that evoked-sustained feedback inhibition is not unique to GC but is present in SGCs as well. Although the amplitude of early evoked IPSCs are not different between the cell types, SGCs receive more frequent basal sIPSCs while GCs show greater enhancement of sustained feedback IPSCs upon afferent activation. These data identify a specific deficit in SGC inhibitory gating following input activation, which likely facilitates their exclusive ability to sustain prolonged firing in response to afferent activation.

Despite studies highlighting the developmental, structural and functional differences between GCs and SGCs (Gupta *et al.*, 2012; Gupta *et al.*, 2020; Save *et al.*, 2018; Williams *et al.*, 2007), the lack of known neurochemical markers to distinguish the cell types leaves morphometric parameters characterized in rats as the only reliable means of distinguishing SGCs from GCs. In this regard, it remains to be determined whether the neuropeptide proenkephalin (PENK), expressed in a subset of prox-1 positive dentate neurons tagged based on increases in the immediate early gene FOS (Erwin *et al.*, 2020), is selective for SGCs or labels highly active neurons regardless of morphology. Our unbiased clustering analysis based on extensive morphometric parameters, and the PCA analysis of features driving clustering of cell types validate the use of number of primary dendrites, dendritic angle, and soma-aspect ratio to distinguish SGCs from GCs. Moreover, dendritic complexity, which could influence intrinsic physiology and input integration (Gulledge et al., 2005; van der Velden et al., 2012; van Elburg and van Ooyen, 2010), was significantly lower in SGCs than in GCs, as reported in rats (Gupta *et*

al., 2020). These data substantiate the use of number of primary dendrites (>3) as a reliable feature to distinguish GCs from SGCs. Curiously, the putative GC cluster segregated into two subclusters, largely driven by differences in dendritic complexity, dendritic angle, and number of primary dendrites with an inverse relation between dendritic complexity and number of primary dendrites. While we did not explore these GC subtypes further, it would be interesting to determine if functional differences in dentate projection neuron subtypes scale with number of primary dendrites and dendritic complexity. Nevertheless, our demonstration of lower input resistance and spike frequency adaptation in SGCs (Fig. 1) as well as the persistent firing (Fig 5A) validate previously reported functional differences between GCs and SGCs (Gupta *et al.*, 2012; Larimer and Strowbridge, 2010; Save *et al.*, 2018; Williams *et al.*, 2007) and justify examination of their role in the dentate circuit.

Consistent with our prior findings in rats (Gupta *et al.*, 2012; Gupta *et al.*, 2020), murine SGCs receive more frequent sIPSCs than GCs. Since SGC somata and dendrites are located in the inner molecular layer, outside the dense axonal arbor of PV-INs in the granule cell layer, we anticipated that SGCs will receive fewer synaptic inputs from PV-INs when compared to GCs. Surprisingly, optogenetic suppression of PV-INs failed to reduce sIPSC frequency in both GCs and SGCs. The inability of NpHR3 mediated suppression PV-INs to reduce GC and SGC sIPSC frequency occurred despite the ability of amber light to reliably suppress firing and elicit membrane hyperpolarization (>5 mV) in YFP positive PV-INs located in the same plane as the recorded GCs and SGCs (Fig. 3 & Fig. S3). Moreover, the stable recordings from PV-INs and ability of optically activated PV-INs to evoke robust increases in principal cell IPSCs confirm the presence of viable, synaptically connected PV-INs. Furthermore, the same amber light protocol reduced evoked sustained IPSCs in SGCs (Fig. 7), demonstrating that NpHR3

suppression of PV-IN firing and IPSCs occurs as expected. Why, then, is PV-IN suppression unable to reduce sIPSCs in GCs and SGCs even in the absence of glutamatergic blockers (Fig. 3) and despite over 80% of sIPSCs being dependent on neuronal firing (Fig. S3F)? One possibility is that optical suppression of PV-INs disinhibits a subset of non-PV interneurons which increase firing and compensate for the loss of PV-IN mediated inhibition. In this regard, the reciprocal activity states of PV and CCK neurons, recently reported in CA1, suggests that such a compensation is possible (Dudok et al., 2021). However, whether such a mechanism would exactly compensate for the reduction in PV-IN mediated IPSCs in a slice is debatable. Moreover, such network-level compensations are unlikely to be resolved by use of alternative optical (archaerhodopsin) or chemogenetic strategies which would suffer from similar confounds. The inherent confound that optical/chemogenetic silencing cannot disambiguate direct from circuit-effects need to be considered while using cell-specific silencing strategies. Our findings raise the possibility that hilar interneurons including dendritically projecting somatostatin neurons, total-molecular layer interneurons and CCK-expressing interneurons as well as diverse populations of molecular layer interneurons may contribute substantively to sIPSCs in GCs and SGCs. While our findings do not imply lack of PV-INs contribution to basal inhibition *in vivo*, the most parsimonious conclusion form our data is that PV-INs have limited role in basal sIPSCs in GCs and SGCs in slices.

PV-INs are known to mediate robust and precise feedforward and feedback inhibition of GCs (Andersen et al., 1966; Ewell and Jones, 2010; Hefft and Jonas, 2005; Kraushaar and Jonas, 2000). Here, we report that optical activation of PV-INs causes robust increase in IPSC frequency in SGCs as well as GCs demonstrating that, despite their location in the inner molecular layer, SGCs receive functional inhibitory synapses from PV-INs. While the maximum

frequency and peak IPSC amplitude in response to optical activation of PV-INs was not different between cell-types, the increase in IPSC frequency, normalized to the basal sIPSC frequency, was substantially lower in SGCs. These findings suggest that the proportion of PV-IN mediated synaptic inhibition in SGCs may be lower than in GCs. However, unlike PP evoked EPSC amplitude which is significantly higher in SGCs than in GCs (Larimer and Strowbridge, 2010), we demonstrate that the amplitude and kinetics of afferent evoked IPSCs were not different between GCs and SGCs. Taken together, these findings suggest that the excitation to inhibition ratio in SGCs in response to afferent activation may be higher and feedback inhibitory gating lower than that in GCs.

Finally, we examined sustained feedback inhibition which was found to correlate with sustained SGC firing and suggested as a mechanism for lateral inhibition (Larimer and Strowbridge, 2010). We confirm that paired suprathreshold PP stimulation elicits persistent SGC firing in about 50% of trials and was temporally correlated with over a two-fold increase in IPSC frequency in both GCs and SGCs. Sustained SGC activity followed the acutely evoke firing by over 200 ms and lasted for over 10s following the stimulation. Interestingly, although individual SGC firing was observed only in half the trials, GCs and/or SGCs showed evoked sustained IPSCs in all slices examined suggesting that activation of a subset of SGCs could support sustained the feedback inhibition of dentate projection neurons. Our recordings identify that about half the YFP-labeled PV-INs examined responded to PP stimulation with increased firing that matched the latency and duration of the sustained SGC firing and evoked sustained inhibition in GCs and SGCs. Notably, two PV-INs which did not exhibit sustained firing showed robust increase in EPSP frequency following paired PP stimulation consistent with enhanced glutamatergic drive. These findings are consistent with recent reports that PV-IN somata receive robust glutamatergic synaptic

innervation exclusively from SGC and not GC axon terminals (Rovira-Esteban *et al.*, 2020). The preferential innervation of PV-IN somata by SGCs (Rovira-Esteban *et al.*, 2020) and temporal correlation between sustained afferent-evoked SGC and PV-IN firing support the proposal that SGC firing drives sustained PV-IN activation.

Although both SGCs and GCs show sustained increase in IPSCs lasting >10s following paired afferent stimulation, we find that the relative increase in IPSC frequency in SGCs is significantly lower than that in GCs. These data indicate that SGCs, while receiving more robust NMDA currents than GCs (Larimer and Strowbridge, 2010), receive less gating feedback inhibition than GCs, placing them in a doubly privileged position to support persistent firing. Indeed, this unique position and the associated persistent firing could contribute to greater expression of activity dependent genes and recruitment of SGCs as part of cellular ensembles with elevated expression of the immediate early gene cFOS in relation to behavioral tasks (Erwin *et al.*, 2020). Our analyses identify selective contribution of PV-INs to sustained feedback inhibition in SGCs but not in GCs. These results are paradoxical, in light of our data demonstrating that the increase in IPSC frequency upon wide field optical activation of PV-INs is significantly lower in SGCs than in GCs (Fig. 4) and raise an intriguing possibility of target specific differences in PV-IN synaptic release and/or short-term plasticity similar to those reported in glutamatergic terminals (Blackman et al., 2013; Eltes et al., 2017; Larsen and Sjostrom, 2015; Sylwestrak and Ghosh, 2012) for future studies.

In conclusion, our study demonstrates an input strength dependent shift in three distinct temporal phases of synaptic inhibition between GCs and SGCs. During steady-state basal activity, SGCs receive greater synaptic inhibitory drive than GCs. In response to afferent activation, evoked synaptic inhibition in SGCs appears comparable to GCs, which, given the greater glutamatergic

inputs reported in SGCs (Larimer and Strowbridge, 2010), represents a relative reduction scaling of inhibition with excitation in SGCs compared to GCs. With further increase in drive during paired stimulation, the increase in sustained feedback inhibition is in SGCs is lower than in GCs. This activity dependent blunting of synaptic inhibitory inputs in SGCs compared to GCs indicates that SGCs, by having reduced activity dependent inhibitory gating, may support a distinct role in dentate processing by integrating, rather than sparsifying, inputs and driving lateral inhibition and selectivity of GCs.

Materials and Methods

Animals: All experiments were performed in accordance with IACUC protocols approved by Rutgers-NJMS, Newark, NJ, and the University of California at Riverside, CA and in keeping with the ARRIVE guidelines. The study included male and female wild-type C57BL/6J (WT) or appropriately validated optogenetic mice (4-8 weeks old, Jackson Laboratory, Bar Harbor, ME). Parvalbumin (PV)-Cre mice (B6;129P2-Pvalbtm1(cre)Arbr/J; JAX #8069) were crossed with either of the two floxed lines (Chr2-YFP: B6;129S-Gt(ROSA)26Sortm32(CAG-COP4*H134R/EYFP)Hze/J; JAX#12569 or NpHR3-YFP: Rosa-CAG-LSL-eNpHR3.0-EYFP-WPRE; JAX #14539) to generate experimental PV-Chr2 and PV-NpHR3 mice. Immunofluorescence labeling for PV and YFP in sections from PV-YFP mice identified that over 80% of PV labeled cells expressed YFP, and all YFP positive cells expressed PV validating the specificity of the PV-cre transgenic lines. Mice were housed with littermates (4 mice per cage) in a 12-h light-dark cycle. Food and water were provided ad libitum.

Slice Physiology: Animals were anesthetized under 3% isoflurane and decapitated. Whole brains were extracted and horizontal brain slices (350 µm) were prepared using Leica VT1000 or VT1200S Vibratomes (Wetzlar, Germany) in ice-cold high Sucrose-aCSF containing (in mM) 85 NaCl, 75 sucrose, 24 $NaHCO_3$, 25 glucose, 4 $MgCl_2$, 2.5 KCl, 1.25 NaH_2PO_4, and 0.5 $CaCl_2$. Sliced were bisected and incubated at 32 ± 1°C for a minimum of 30 min in a submerged holding chamber containing recording aCSF and subsequently held at room temperature (RT, 22-23°C). The recording aCSF contained (in mM) 126 NaCl, 2.5 KCl, 2 $CaCl_2$, 2 $MgCl_2$, 1.25 NaH_2PO_4, 26 $NaHCO_3$ and 10 D-glucose. All solutions were saturated with 95% O_2 and 5% CO_2 and maintained at a pH of 7.4 for 2-6 h (Gupta *et al.*, 2012; Yu et al., 2016).

Slices (350 µm) were transferred to a submerged recording chamber and perfused with oxygenated aCSF at 33 ± 1°C. Whole-cell voltage- and current-clamp recordings from GCs, SGCs and presumed interneurons at the border of the hilus and GCL were performed under IR-DIC visualization with a Nikon Eclipse FN-1 (Nikon Corporation, Shinagawa, Tokyo, Japan) or Olympus BX50 (Olympus Corporation, Shinjuku, Tokyo, Japan) microscope, using 40X water-immersion objectives. Recordings were obtained using Axon Instruments Axopatch 200B or MultiClamp 700B amplifiers (Molecular Devices, Sunnyvale, CA). Data were obtained using glass microelectrodes (3–5 MΩ) pulled using a Narishige PC-10 puller (Narishige Japan, Tokyo, Japan) or Sutter P-1000 Glass puller (Sutter Instruments, Novato, CA) and were low-pass filtered at 3 kHz, digitized using DigiData 1440A and acquired using pClamp10 at 10-kHz sampling frequency with gains of 0.1 and 1. Recordings were performed using high chloride internal solution containing (in mM) 125 KCl, 10 K-gluconate, 10 HEPES, 2 $MgCl_2$, 0.2 EGTA, 2 Na-ATP, 0.5 Na-GTP and 10 PO Creatine titrated to a pH 7.25 with KOH (pH 7.25; 270–290 mOsm) or cesium methane sulfonate ($CsMeSO_4$) internal solution containing (in mM) 140 cesium methane sulfonate, 10 HEPES, 5 NaCl, 0.2 EGTA, 2 Mg-ATP, 0.2 Na-GTP (pH 7.25; 270–290 mOsm). Biocytin (0.3%) was included in the internal solution for post-hoc cell identification (Gupta *et al.*, 2012; Yu et al., 2015). In experiments with KCl based internal, synaptic GABA currents were recorded in perfusing aCSF containing the glutamate receptor antagonist kynurenic acid (3 mM, Tocris, Ellisville, MO). Recorded neurons were initially held at -70 mV for interneurons and -60 mV for GCs and SGCs and the response to 500 milli-second positive and negative current injections were examined to determine active and passive characteristics. Voltage Clamp recordings of IPSCs (spontaneous and evoked) were obtained from a holding potential of -70 mV for interneurons and -60 mV for GCs and SGCs (Gupta *et*

al., 2020; Yu *et al.*, 2015). $CsMeSO_4$ based internal was used to record the IPSCs as outward currents from a holding potential of at 0 mV in the absence of glutamate receptor antagonists. In some experiments tetrodotoxin (TTX, 1 μM) or gabazine (10 μM) were used to isolate action potential independent miniature IPSCs or block IPSCs, respectively. Post-hoc biocytin immunostaining and morphological analysis was used to definitively identify interneurons, GCs and SGCs included in this study. Morphologies were reconstructed for further analysis.

Evoked IPSCs were elicited by stimulation of the PP using bipolar concentric stimulating electrodes placed at the junction of the dorsal blade and the crest, just outside the fissure (Korgaonkar et al., 2020). Constant current stimuli (0.5 μA-5 mA) were applied using a high-voltage stimulus isolator (A365R, World Precision Instruments, Sarasota, FL). The evoked mono and polysynaptic IPSCs were recorded simultaneously in GCs and SGC pairs. In some experiments, slices from were exposed to wide-field blue (λ=470nm) or amber (λ=589nm, 10 mW/mm^2) illumination using Lambda DG-4 Plus (Sutter Instruments, Novato, CA) or Thorlabs 4-Wavelength High-Power LED Sources (Thorlabs, Newton, NJ).

Immunohistochemistry: Following physiological recordings, slices were fixed in 0.1mM phosphate buffer containing 4 % paraformaldehyde at 4°C. For *post-hoc* immunohistochemistry, slices were incubated overnight at 4°C with Alexa Fluor 594-conjugated streptavidin in 0.3% Triton X-100 and 2% normal goat serum containing PBS. Slices were mounted on glass slides using vectashield. Sections were visualized and imaged using a Zeiss LSM 510 confocal microscope with a 0.5 numerical aperture 20× objectives.

Morphometry: Stained hippocampal sections were visualized and imaged using a Nikon A1R laser scanning confocal microscope with a 20X, 0.5 NA objective lens. Cell reconstructions,

from confocal image stacks, were performed using the directional kernels user-guided reconstruction algorithm in Neurolucida 360 (MBF Bioscience) followed by manual correction and validation in 3D. About 10-20 percent of each dendritic arbor was reconstructed manually(Gupta *et al.*, 2020). Algorithms in Neurolucida Explorer (MBF Biosciences) were used to extract nonnominal or nonordinal somatodendritic morphological quantitative parameters for use in statistical comparisons and hierarchical cluster analysis. A total of 17 projection neurons in which the dendritic arbors were fully reconstructed were analyzed. A total of 42 somato-dendritic parameters from 17 morphologically reconstructed neurons, including both features measured in Neurolucida Explorer from the 3D reconstructions and parameters measured manually in 2D rendering (Neurolucida 360, MicroBrightfield) were analyzed.

Quantification and Statistical Analysis: Data were tested for uniform distribution and each quantified variable was fit to the sum of two or more Gaussian functions and quality of fit determined using maximum likelihood analysis (MLA; v2test) to assess normal distribution of parameters within each cell type. Variables with a nonuniform distribution were used for subsequent cluster analysis. Hierarchical cluster analysis on principal components (HCPC) of morphological parameters was conducted using R version 3.5.0, using R package FactoMineR by an investigator (H. X) blinded to cell types and age groups. Hierarchical clustering on the selected principal components was performed using Ward's criterion with Euclidean distance to generate the dendrogram. The clustering partition was obtained from hierarchical clustering and improved with K-means method (Husson et al., 2010).

Individual spontaneous, miniature and evoked IPSCs were detected using custom software in IgorPro7.0 (WaveMetrics, Lake Oswego, OR) and different parameters were analyzed (Gupta *et al.*, 2012). Events were visualized, and any "noise" that spuriously met trigger specifications was

rejected. EPSCs were detected and analyzed using event detection in Clampfit. Cumulative probability plots of sIPSC amplitude and frequency were constructed using IgorPro by pooling an equal number of sIPSCs from each cell. Kinetics and charge transfer were calculated from the averaged trace of all accepted sIPSC events. Rise time was measured as the time for amplitude to change from 20 to 80 % of peak. Amplitude weighted τ_{decay} was calculated from a two-exponential fit to the IPSC decay. sIPSC charge transfer was calculated as the area under the curve of the baseline adjusted average sIPSC trace. Intrinsic properties were extracted by analyzing the IV traces in Clampfit. Input resistance was calculated in response to -100 pA current injection. Spike frequency adaptation ratio was calculated as interval between the first two spikes/interval between the two last spikes in response to +70 pA current injection. Sample sizes were not predetermined and conformed with those employed in the field. Significance was set to $p<0.05$, subject to appropriate Bonferroni correction. Statistical analysis was performed by paired and unpaired Student's *t* test (Microsoft Excel 2007) or Two-way repeated measures ANOVA, One-way ANOVA or One-way ANOVA on Ranks followed by Pairwise Multiple Comparison using Holm-Sidak method or Dunn's method (Sigma Plot 12.3) as appropriate. Data are shown as mean±SEM (standard error of the mean) or median and interquartile range (IQR) where appropriate**.**

Acknowledgements

We thank Dr. Luke Fritzky at the Rutgers Imaging Core for help with imaging, Dr. Archana Proddutur for immunostaining validation of transgenic mouse lines and Dr. Deepak Subramanian for developing schematics. The project was supported by NIH/NINDS R01 NS069861, R01NS097750 and NJCBIR CBIR16IRG017 to V.S., NJCBIR CBIR15FEL011 to M.A and CBIR11FEL003 to A.G.

Author Contributions: M.A., B.S performed experiments; M.A., A.G. and H.X. analyzed data; M.A., H.X., and V.S. interpreted results of experiments; M.A., prepared figures; M.A. and V.S. conceived of and designed research; M.A., and V.S. drafted manuscript.

Competing Interests: The authors declare no competing interests.

Reference List

Alfonsa, H., Merricks, E.M., Codadu, N.K., Cunningham, M.O., Deisseroth, K., Racca, C., and Trevelyan, A.J. (2015). The contribution of raised intraneuronal chloride to epileptic network activity. J Neurosci *35*, 7715-7726. 10.1523/JNEUROSCI.4105-14.2015.

Andersen, P., Holmqvist, B., and Voorhoeve, P.E. (1966). Entorhinal activation of dentate granule cells. Acta Physiol Scand *66*, 448-460. 10.1111/j.1748-1716.1966.tb03223.x.

Arima-Yoshida, F., Watabe, A.M., and Manabe, T. (2011). The mechanisms of the strong inhibitory modulation of long-term potentiation in the rat dentate gyrus. Eur J Neurosci *33*, 1637-1646. 10.1111/j.1460-9568.2011.07657.x.

Bekinschtein, P., Kent, B.A., Oomen, C.A., Clemenson, G.D., Gage, F.H., Saksida, L.M., and Bussey, T.J. (2013). BDNF in the dentate gyrus is required for consolidation of "pattern-separated" memories. Cell Rep *5*, 759-768. 10.1016/j.celrep.2013.09.027.

Blackman, A.V., Abrahamsson, T., Costa, R.P., Lalanne, T., and Sjostrom, P.J. (2013). Target-cell-specific short-term plasticity in local circuits. Front Synaptic Neurosci *5*, 11. 10.3389/fnsyn.2013.00011.

Braganza, O., Mueller-Komorowska, D., Kelly, T., and Beck, H. (2020). Quantitative properties of a feedback circuit predict frequency-dependent pattern separation. Elife *9*. 10.7554/eLife.53148.

Dengler, C.G., and Coulter, D.A. (2016). Normal and epilepsy-associated pathologic function of the dentate gyrus. Prog Brain Res *226*, 155-178. 10.1016/bs.pbr.2016.04.005.

Dudok, B., Klein, P.M., Hwaun, E., Lee, B.R., Yao, Z., Fong, O., Bowler, J.C., Terada, S., Sparks, F.T., Szabo, G.G., et al. (2021). Alternating sources of perisomatic inhibition during behavior. Neuron *109*, 997-1012 e1019. 10.1016/j.neuron.2021.01.003.

Eltes, T., Kirizs, T., Nusser, Z., and Holderith, N. (2017). Target Cell Type-Dependent Differences in Ca(2+) Channel Function Underlie Distinct Release Probabilities at Hippocampal Glutamatergic Terminals. J Neurosci *37*, 1910-1924. 10.1523/JNEUROSCI.2024-16.2017.

Erwin, S.R., Sun, W., Copeland, M., Lindo, S., Spruston, N., and Cembrowski, M.S. (2020). A Sparse, Spatially Biased Subtype of Mature Granule Cell Dominates Recruitment in Hippocampal-Associated Behaviors. Cell Rep *31*, 107551. 10.1016/j.celrep.2020.107551.

Ewell, L.A., and Jones, M.V. (2010). Frequency-tuned distribution of inhibition in the dentate gyrus. The Journal of neuroscience : the official journal of the Society for Neuroscience *30*, 12597-12607. 10.1523/JNEUROSCI.1854-10.2010.

Freund, T.F., and Buzsaki, G. (1996). Interneurons of the hippocampus. Hippocampus *6*, 347-470.

GoodSmith, D., Chen, X., Wang, C., Kim, S.H., Song, H., Burgalossi, A., Christian, K.M., and Knierim, J.J. (2017). Spatial Representations of Granule Cells and Mossy Cells of the Dentate Gyrus. Neuron *93*, 677-690 e675. 10.1016/j.neuron.2016.12.026.

Gulledge, A.T., Kampa, B.M., and Stuart, G.J. (2005). Synaptic integration in dendritic trees. J Neurobiol *64*, 75-90. 10.1002/neu.20144.

Gupta, A., Elgammal, F.S., Proddutur, A., Shah, S., and Santhakumar, V. (2012). Decrease in tonic inhibition contributes to increase in dentate semilunar granule cell excitability after brain injury. J Neurosci *32*, 2523-2537. 10.1523/JNEUROSCI.4141-11.2012.

Gupta, A., Proddutur, A., Chang, Y.J., Raturi, V., Guevarra, J., Shah, Y., Elgammal, F.S., and Santhakumar, V. (2020). Dendritic morphology and inhibitory regulation distinguish dentate semilunar granule cells from granule cells through distinct stages of postnatal development. Brain Struct Funct *225*, 2841-2855. 10.1007/s00429-020-02162-y.

Hainmueller, T., and Bartos, M. (2020). Dentate gyrus circuits for encoding, retrieval and discrimination of episodic memories. Nat Rev Neurosci *21*, 153-168. 10.1038/s41583-019-0260-z.

Hefft, S., and Jonas, P. (2005). Asynchronous GABA release generates long-lasting inhibition at a hippocampal interneuron-principal neuron synapse. Nat.Neurosci. *8*, 1319-1328.

Hefft, S., Kraushaar, U., Geiger, J.R., and Jonas, P. (2002). Presynaptic short-term depression is maintained during regulation of transmitter release at a GABAergic synapse in rat hippocampus. J Physiol *539*, 201-208.

Heinemann, U., Beck, H., Dreier, J.P., Ficker, E., Stabel, J., and Zhang, C.L. (1992). The dentate gyrus as a regulated gate for the propagation of epileptiform activity. Epilepsy Res.Suppl *7*, 273-280.

Howard, A., Tamas, G., and Soltesz, I. (2005). Lighting the chandelier: new vistas for axo-axonic cells. Trends Neurosci. *28*, 310-316.

Husson, F., Josse, J., and Pages, J. (2010). Principal component methods - hierarchical clustering - partitional clustering: why would we need to choose for visualizing data? September 2010. https://pdfs.semanticscholar.org/0433/5d99d840ac3370f5aeb262828cf127d3ff1c.pdf?_ga=2.221145628.586236108.1558133524-1373605863.1558133524.

Korgaonkar, A.A., Li, Y., Sekhar, D., Subramanian, D., Guevarra, J., Swietek, B., Pallottie, A., Singh, S., Kella, K., Elkabes, S., and Santhakumar, V. (2020). Toll-like Receptor 4 Signaling in Neurons Enhances Calcium-Permeable alpha-Amino-3-Hydroxy-5-Methyl-4-Isoxazolepropionic Acid Receptor Currents and Drives Post-Traumatic Epileptogenesis. Ann Neurol *87*, 497-515. 10.1002/ana.25698.

Kraushaar, U., and Jonas, P. (2000). Efficacy and stability of quantal GABA release at a hippocampal interneuron-principal neuron synapse. J Neurosci *20*, 5594-5607.

Larimer, P., and Strowbridge, B.W. (2010). Representing information in cell assemblies: persistent activity mediated by semilunar granule cells. Nat Neurosci *13*, 213-222. 10.1038/nn.2458.

Larsen, R.S., and Sjostrom, P.J. (2015). Synapse-type-specific plasticity in local circuits. Curr Opin Neurobiol *35*, 127-135. 10.1016/j.conb.2015.08.001.

Lothman, E.W., Stringer, J.L., and Bertram, E.H. (1992). The dentate gyrus as a control point for seizures in the hippocampus and beyond. Epilepsy Res.Suppl *7*, 301-313.

Ramón y Cajal, S. (1995). Histology of the nervous system of man and vertebrates (Oxford University Press).

Rovira-Esteban, L., Hajos, N., Nagy, G.A., Crespo, C., Nacher, J., Varea, E., and Blasco-Ibanez, J.M. (2020). Semilunar Granule Cells Are the Primary Source of the Perisomatic Excitatory Innervation onto Parvalbumin-Expressing Interneurons in the Dentate Gyrus. eNeuro *7*. 10.1523/ENEURO.0323-19.2020.

Santhakumar, V. (2008). Modeling mossy cell loss and mossy fiber sprouting in epilepsy. In Computational Neuroscience in Epilepsy, I. Soltesz, and K.J. Staley, eds. (Academic Press), pp. 89-111.

Save, L., Baude, A., and Cossart, R. (2018). Temporal Embryonic Origin Critically Determines Cellular Physiology in the Dentate Gyrus. Cereb Cortex. 10.1093/cercor/bhy132.

Sik, A., Penttonen, M., and Buzsaki, G. (1997). Interneurons in the hippocampal dentate gyrus: an in vivo intracellular study. European Journal of Neuroscience *9*, 573-588.

Soltesz, I., Smetters, D.K., and Mody, I. (1995). Tonic inhibition originates from synapses close to the soma. Neuron *14*, 1273-1283.

Stell, B.M., Brickley, S.G., Tang, C.Y., Farrant, M., and Mody, I. (2003). Neuroactive steroids reduce neuronal excitability by selectively enhancing tonic inhibition mediated by delta subunit-containing GABAA receptors. Proc Natl Acad Sci U S A *100*, 14439-14444. 10.1073/pnas.2435457100.

Sylwestrak, E.L., and Ghosh, A. (2012). Elfn1 regulates target-specific release probability at CA1-interneuron synapses. Science *338*, 536-540. 10.1126/science.1222482.

van der Velden, L., van Hooft, J.A., and Chameau, P. (2012). Altered dendritic complexity affects firing properties of cortical layer 2/3 pyramidal neurons in mice lacking the 5-HT3A receptor. J Neurophysiol *108*, 1521-1528. 10.1152/jn.00829.2011.

van Elburg, R.A., and van Ooyen, A. (2010). Impact of dendritic size and dendritic topology on burst firing in pyramidal cells. PLoS Comput Biol *6*, e1000781. 10.1371/journal.pcbi.1000781.

Walker, M.C., Pavlov, I., and Kullmann, D.M. (2010). A 'sustain pedal' in the hippocampus? Nature neuroscience *13*, 146-148. 10.1038/nn0210-146.

Williams, P.A., Larimer, P., Gao, Y., and Strowbridge, B.W. (2007). Semilunar granule cells: glutamatergic neurons in the rat dentate gyrus with axon collaterals in the inner molecular layer. J Neurosci *27*, 13756-13761. 10.1523/JNEUROSCI.4053-07.2007.

Yu, J., Proddutur, A., Swietek, B., Elgammal, F.S., and Santhakumar, V. (2016). Functional Reduction in Cannabinoid-Sensitive Heterotypic Inhibition of Dentate Basket Cells in Epilepsy: Impact on Network Rhythms. Cereb Cortex *26*, 4229-4314. 10.1093/cercor/bhv199.

Yu, J., Swietek, B., Proddutur, A., and Santhakumar, V. (2015). Dentate total molecular layer interneurons mediate cannabinoid-sensitive inhibition. Hippocampus *25*, 884-889. 10.1002/hipo.22419.

Supplementary Figures

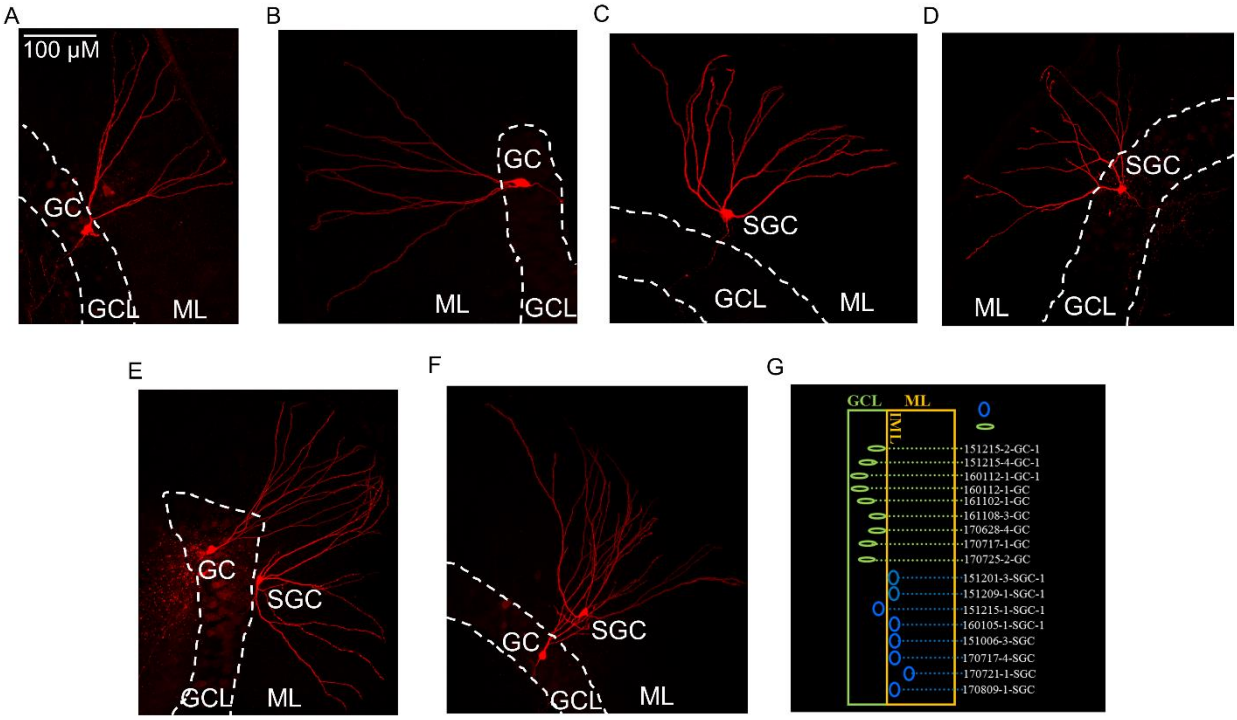

Figure S1: Representative images and somatic location of GCs and SGCs. A-F. Example images of GCs (A-B) and SGCs (C-D) and GC-SGC pairs (E-F) recorded during dual recordings illustrate the somatic location and dendritic spread. Note that reconstruction of neuron in A is presented in Fig 1A and panels E and F are presented in Fig 5G and 7C, respectively. Scale bar: 100µm; G. Schematic of the somatic location of the cells included in the cluster analysis. The GCL is illustrated as a green box and IML as an orange box with somata illustrated in blue and GCs in green. All images were obtained a 20X magnification. GCL: Granule Cell Layer, IML: Inner Molecular Layer.

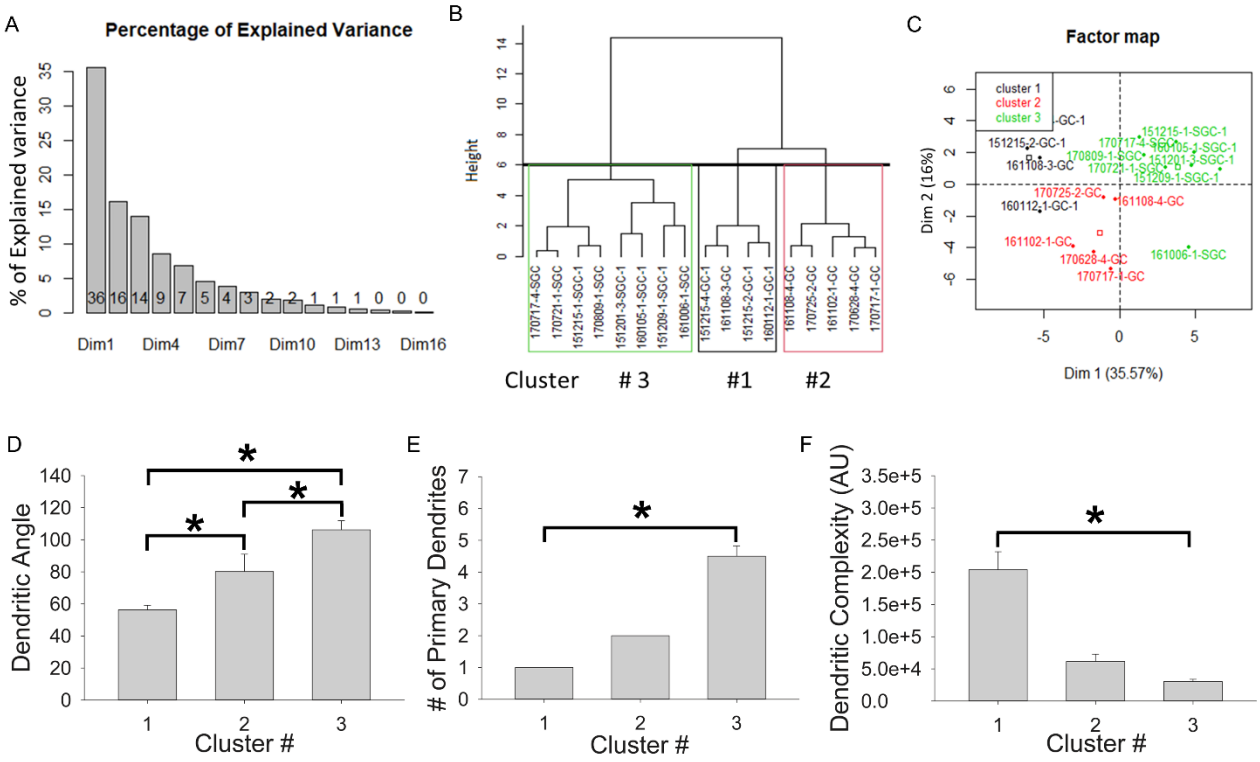

Figure S2: Analysis of Morphological Variables underlying Principal Components. A. Histogram illustrates percentage of information retained by each dimension (principal component, PC). B. Dendrogram generated by Hierarchical Clustering on Principal Components (HCPC) based on 42 morphometric parameters (Supplementary Tables 1 & 2) using Ward's method with Euclidean distance suggests three putative clusters. C. Factor map base on first 7 PCs. D-F. Summary data of dendritic angle (D), number of primary dendrites (E) and Dendritic Complexity (F) for cells in the three clusters. Data are presented as mean±sem. * indicates $p<0.05$ by One-way ANOVA followed by pairwise comparison with Holm-Sidak method for D and $p<0.05$ by One-way ANOVA on Ranks followed by pairwise comparison with Dunn's method for E and F where the data failed Shapiro-Wilk Normality Test. A. U: Arbitrary Units.

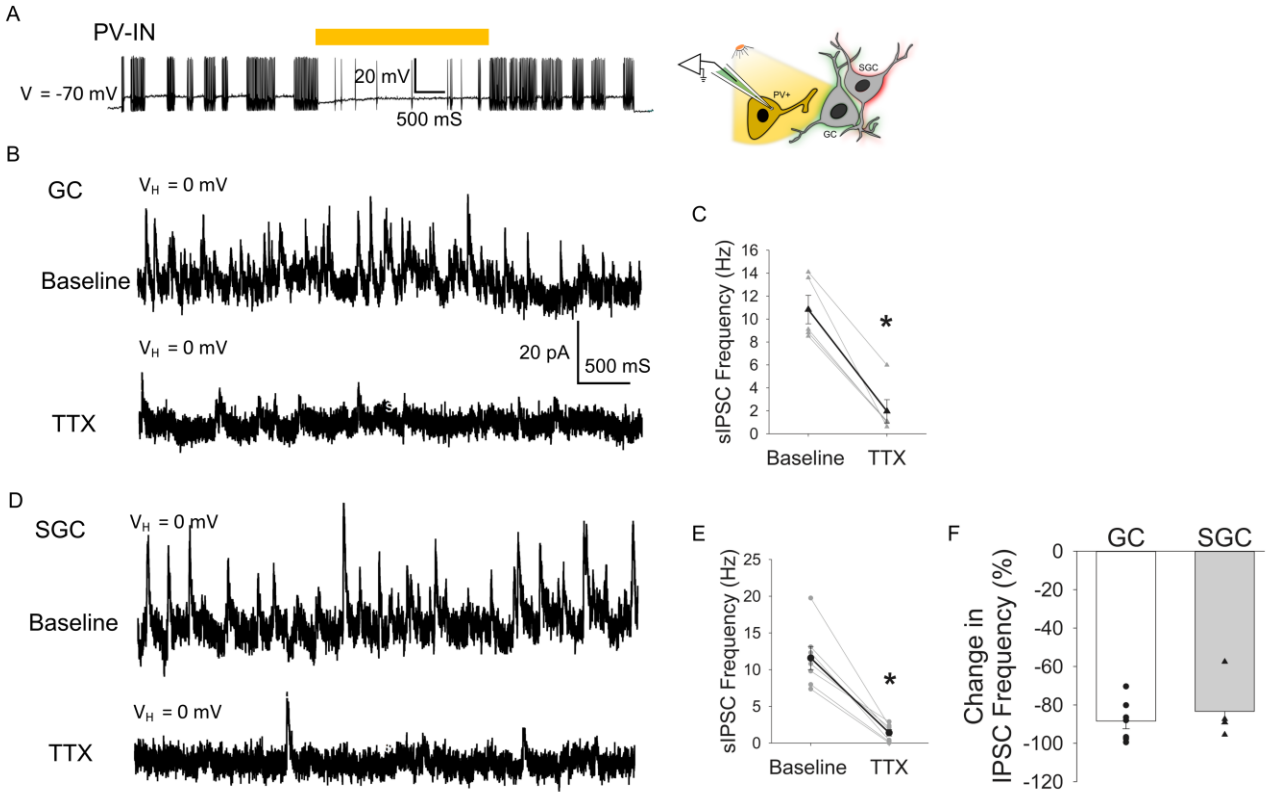

Figure S3: Action potential dependence of GC and SGC sIPSCs. A. Representative membrane voltage trace from a holding potential of -70 mV in a YFP-positive PV interneuron expressing halorhodopsin in the granule cell-hilar border illustrates the high frequency firing during depolarizing current injection (100 pA for 10 sec) and the ability of amber light (bar above) to suppress firing. Representative trace from 19 trials in 4 cells. Schematic to the right illustrates recording condition and optical stimulation. B. Current traces from a GC recorded from a holding potential of 0 mV illustrates sIPSCs recorded in ACSF (baseline above) and miniature IPSCs in TTX (below) (B). C. Summary plot of IPSC frequency in ACSF and TTX in GCs (N=7). D. Example voltage clamp traces from an SGC recorded from a holding potential of 0 mV illustrates sIPSCs recorded in ACSF (baseline above) and miniature IPSCs in TTX (below) (B). E. Summary plot of IPSC frequency in ACSF and TTX in SGCs (n=5) (D). E) Summary plot showing the percent reduction in IPSC frequency in TTX. * indicates $p<0.05$ by paired t-test. Data presented as mean±sem.

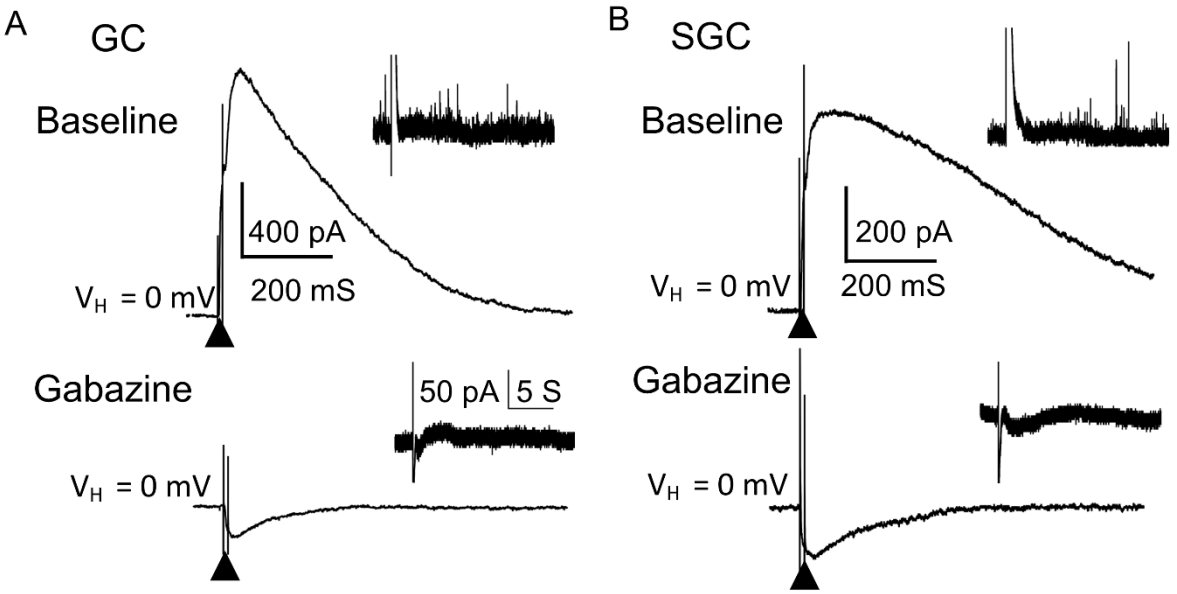

Figure S4: $GABA_AR$ dependence of both early and sustained perforant path evoked IPSCs. A-B. Representative traces illustrate IPSC in a GC (A) and an SGC (B) evoked by a pair of suprathreshold perforant path stimuli at 10 ms interval (above) and the block in the $GABA_AR$ antagonist gabazine (10 µM) (below). Insets on a different scale show the evoked sustained activity (above) is also blocked by gabazine (below). Based on recordings from 2 cells each.

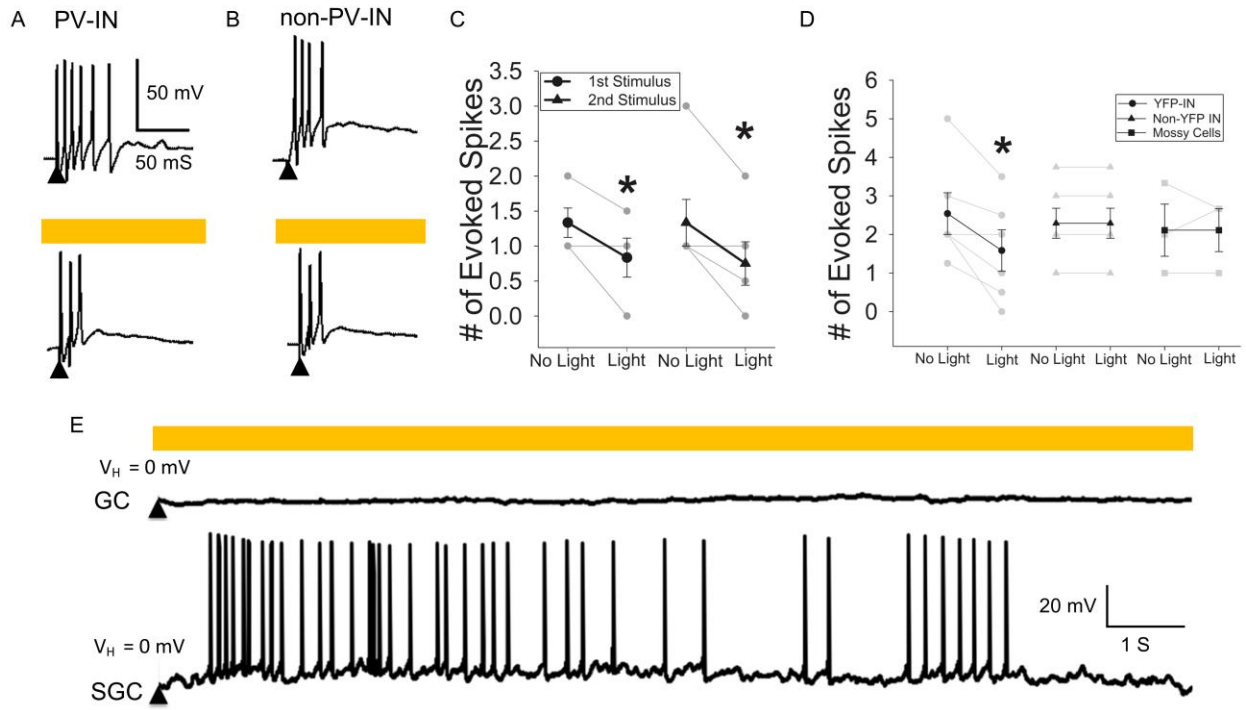

Figure S5: Cell specificity of halorhodopsin suppression of PV neuron firing. A. Representative membrane voltage traces from a YFP-positive PV interneuron expressing halorhodopsin in the granule cell-hilar border in response to a pair of suprathreshold perforant path stimuli at 10 ms interval illustrated the early evoked firing in PV neurons (above). Effect of amber light exposure on perforant path evoked PV-IN firing is illustrated (below). B. Example voltage traces from a YFP-negative hilar neuron in response to a pair of suprathreshold perforant path stimuli at 10 ms interval (above). Effect of amber light exposure on perforant path hilar neuron firing is illustrated (below). C. Summary data of number of spikes elicited following the first and second stimuli and the effect of halorhodopsin activation on perforant path evoked firing in PV-IN. D. Summary plot compares the effect of amber light on afferent evoke firing in halorhodopsin expressing PV-IN and YFP-negative presumed hilar interneurons and mossy cells. Mossy cells were identified based on the presence of large multipolar somata and thorny excrescences in biocytin cell fills. * indicates $p<0.05$ by paired t-test. Data presented as mean±sem. E. Representative traces show lack of sustained firing in GCs and sustained firing in SGCs following paired suprathreshold perforant path stimulation.

Supplementary Tables

Table S1: Definition of somatic morphological parameters modified from Gupta et al., 2020

Parameter	Acronym	Equations	Definitions: MBF BIOSCIENCE , Williston, VT USA
Surface Area	*Sarea*	[(Perimeter Contour 1 + Perimeter Contour 2 + ... + Perimeter Contour n)/n] * Thickness	Addition of outer surface area of stack of all the contours
Volume	*Svol*	N/A	Calculations for the cell body were accomplished by dividing the soma into stacks with equal thickness and quantifying the summed volume of the
Width	*Swith*	N/A	Measure of the largest distance in soma parallel to the hilar border
Somatic parameters related to largest soma cross section based on highest perimeter			
Aspect Ratio	*S_Asp_Rt*	N/A	This is a 2D parameter of soma contour defined as the ratio of its minimum diameter to its maximum diameter. [Range of values is 0-1. A circle has an aspect ratio of 1]
Compactness	*S_cmpct*	SQRT(4π*Area)/ Max Diameter	2D parameter describes the relationship between the area and the maximum diameter. [Range of values is 0 to 1. A circle is the most compact
Contour	*Cont*	N/A	Each slice division of the soma
Convexity	*S_xity*	Convex Perimeter/Perimeter	A completely convex object does not have indentations, and has a convexity value of 1 (e.g., circles, ellipses, and squares). Concave objects have convexity values less than 1
Feret Max	*Feret.X*	N/A	The largest dimensions of the contour as if a caliper was used to measure across the contour
Form Factor	*S_Form*	$(4\pi*\text{Area})/(\text{Perimeter})^2$	The form factor differs from the compactness by considering the complexity of the perimeter of the object. As the contour shape approaches that of a perfect circle, this value approaches a maximum of 1.0
Perimeter	*Speri*	Perimeter +/- (Perimeter Error Coefficient * Max distance from contour boundary in microns)	Refers to the length of the contour for either open or closed contours. The length takes the Z positions of the coordinates into account
Roundness	*S_Rnd*	$[\text{Compactness}]^2$	Roundness is the square of the compactness to enable discrimination of objects with small compactness values
Solidity	*S_solid*	Area/Convex Area	Solidity is the area of the contour divided by the convex area. The area enclosed by a 'rubber band' stretched around a contour is called the convex area. Circles, squares, and ellipses have a solidity of 1. Indentations in the contour take area away from the convex area, decreasing the actual area within the contour. Note that it is possible to have contours with low convexity and high solidity, vice versa

Table S2: Definition of dendritic morphological parameters modified from Gupta et al., 2020

Parameter	Acronym	Equations	Definitions: MBF BIOSCIENCE , Williston, VT USA
Angle	*ang*	N/A	Two dimensional measurement of angle subtended by the most distal of the most distant dendrites at the center of soma
Centrifugal Ordering and Branch Orders	*N/A*	N/A	The centrifugal ordering scheme is used to assign branch order to a tree. The segment that begins at the origin of the dendrite is assigned the branch order 1. The branches that connect to that segment are assigned the branch order 2 and so on until all branches are assigned a value.
Dendritic Complexity	*D_Cmplx*	[Sum of the Terminal Oders + Number of Terminals] * [Total Dendritic Length / Number of Primary Dendrites]	A parameter that normalizes and compares distribution of dendrites among fundamentally different neurons
Dendritic Length	*D_Lth*	x1lth + x2lth + x3lth…….	Total length of all the dendrites
Dendritic Mean Length	*D_MnLth*	D_Lth / # of Primary Dendrites	Length per dendritic tree arising from soma
Maximum Order	*MxOrdr*	N/A	Maximum order up to which dendritic segments reach
Primary	*prim*	N/A	Number of dendrites originating directly from soma
Primary, Secondary tertiary length	*x1lth, x2lth, x3lth*	N/A	Summed lengths of all segments in a given dendritic order
Primary Secondary, Tertiary, Quaternary Dendritic Segments	*x1segm, x2segm, x3segm & x4segm*	N/A	Number of dendritic segments in first, second, third and fourth order dendrites respectively. Note X1SEGM is the same as PRIM
Space Volume of Cell	*D_Area*	Convex Hull	Volume of the space occupied by the dendritic arbors of the cell
Surface Area of Space Occupied by Cell	*D_Volume*	Convex Hull	Surface area of the space occupied by the dendritic arbors of the cell
Tortuosity	*Tort*	Tortuosity = [Distance Along Process] / [Straight Line Distance]	The smallest tortuosity possible is 1—This is a straight path. Tortuosity increases as the segment assumes a more complex path to reach its destination. Tortuosity allows segments of different lengths to be compared in terms of the complexity of the paths they take
Totals Terminals, Primary Secondary, Tertiary, Quaternary Terminals	*end, x1end, x2end, x3end & x4end*	N/A	Number of distal ends or terminals of dendritic segments that don't divide further

Table S3: Summary data of plots included in figures. Data are presented as mean±sem or median (interquartile range) as appropriate.

		Groups			
Figure #	**Unit**	**GC**		**SGC**	
1B	Count	16.90±1.13		16.87±0.81	
1C	Degree	69.00±5.98		106.23±5.71	
1D	μM	2147.37±128.20		2269.97±126.30	
1E	Count	1.50±0.17		4.5±0.33	
1F	Ratio	0.60±0.05		1.08±0.13	
1G	A.U.	143653.30±26506.76		30290.86±3515.42	
1J	MΩ	309.89±19.58		229.33±29	
1K	Ratio	0.45±0.05		0.68±0.07	
2C	Hz	8.38±1.14		13.63±1.10	
2D	pA	42.98±3.35		40.19±2.78	
2E	mS	3.31±0.22		3.20±0.20	
2F	mS	0.215±0.006		0.204±0.004	
4D	%	719.12±141.61		355.58±40.16	
		GC-No Light	**GC-Light**	**SGC-No Light**	**SGC-Light**
3D	Hz	14.19±2.53	13.61±2.35	15.62 ±2.60	14.69±2.01
3E	pA	46.65 ±9.62	45.13±9.54	43.18 ±5.09	40.95±3.20
3G	Hz	26.80±3.78	28.32±2.41	35.77±5.44	36.81±4.48
3H	pA	26.43±2.88	25.46±2.10	28.96±3.72	26.74±3.17
4C	Hz	8.45±1.31	52.11±5.92	13.37±1.20	57.36±4.92
7D	%	264.59±49.76	225.85±43.09	209.76±57.92	127.86±41.15
		SGC			
5C	S	1.14 (0.61 - 1.90)			
5D	S	15.546±1.28			
		SGC		**PV-IN**	
6C	S	1.14 (061 - 1.90)		1.03 (0.62 - 2.03)	

Table S4: Statistical analysis for data in figures.

Figure #	Test	N (raw)	N (definition)	Descriptive Stats	P Value	Degrees of Freedom
1B	Student's T-Test (Independent)	GC=10 SGC=8	Number of Cells from 8 Animals (GC & SGC)	Bars: Average Error Bars : S.E.M.	0.986	N/A
1C	Student's T-Test (Independent)	GC=10 SGC=8	Number of Cells from 8 Animals (GC & SGC)	Bars: Average Error Bars : S.E.M.	0.0004	N/A
1D	Student's T-Test (Independent)	GC=10 SGC=8	Number of Cells from 8 Animals (GC & SGC)	Bars: Average Error Bars : S.E.M.	0.512	N/A
1E	Student's T-Test (Independent)	GC=10 SGC=8	Number of Cells from 8 Animals (GC & SGC)	Bars: Average Error Bars : S.E.M.	1.9E-07	N/A
1F	Student's T-Test (Independent)	GC=10 SGC=8	Number of Cells from 8 Animals (GC & SGC)	Bars: Average Error Bars : S.E.M.	0.001	N/A
1G	Student's T-Test (Independent)	GC=10 SGC=8	Number of Cells from 8 Animals (GC & SGC)	Bars: Average Error Bars : S.E.M.	0.002	N/A
1I	Two Way RM ANOVA	GC=8 SGC=10	Number of Cells from 7 Animals (GC & SGC)	Black Circles and Triangles: Average	0.876	F(1,16)=0.025
1J	Student's T-Test (Independent)	GC=18 SGC=19	Number of Cells from 12 (GC) and 13 (SGC) Animals	Bars: Average Error Bars : S.E.M.	0.031	N/A
1K	Student's T-Test (Independent)	GC=16 SGC=19	Number of Cells from 12 (GC) and 13 (SGC) Animals	Bars: Average Error Bars : S.E.M.	0.023	N/A
2C	Student's T-Test (Independent)	GC=18 SGC=19	Number of Cells from 12 (GC) and 13 (SGC) Animals	Bars: Average Error Bars : S.E.M.	0.003	N/A
2D	Student's T-Test (Independent)	GC=18 SGC=19	Number of Cells from 12 (GC) and 13 (SGC) Animals	Bars: Average Error Bars : S.E.M.	0.748	N/A
2E	Student's T-Test (Independent)	GC=17 SGC=14	Number of Cells from 12 (GC) and 13 (SGC) Animals	Bars: Average Error Bars : S.E.M.	0.721	N/A
2F	Student's T-Test (Independent)	GC=17 SGC=14	Number of Cells from 12 (GC) and 13 (SGC) Animals	Bars: Average Error Bars : S.E.M.	0.126	N/A
3D	Student's T-Test (Paired)	GC=5 SGC=5	Number of Cells from 3 (GC) and 4 (SGC) Animals	Black Circles and Triangles: Average Error Bars: S.E.M.	GC: 0.605 SGC: 0.785	N/A
3E	Student's T-Test (Paired)	GC=5 SGC=5	Number of Cells from 3 (GC) and 4 (SGC) Animals	Black Circles and Triangles: Average Error Bars: S.E.M.	GC: 0.421 SGC: 0.420	N/A
3G	Student's T-Test (Paired)	GC=13 SGC=11	Number of Cells from 8 Animals (GC & SGC)	Black Circles and Triangles: Average Error Bars: S.E.M.	GC: 0.487 SGC: 0.659	N/A
3H	Student's T-Test (Paired)	GC=13 SGC=11	Number of Cells from 8 Animals (GC & SGC)	Black Circles and Triangles: Average Error Bars: S.E.M.	GC: 0.759 SGC: 0.247	N/A
4C	Student's T-Test (Paired)	GC=14 SGC=14	Number of Cells from 8 (GC) and 9 (SGC) Animals	Black Circles and Triangles: Average Error Bars: S.E.M.	GC: 2.74E-06 SGC: 2.38E-07	N/A
4D	Student's T-Test (Independent)	GC=14 SGC=14	Number of Cells from 8 (GC) and 9 (SGC) Animals	Bars: Average Error Bars : S.E.M.	0.020	N/A
4G	Two Way RM ANOVA	GC=5 SGC=7	Number of Cells from 4 Animals (GC & SGC)	Black Circles and Triangles: Average	0.372	F(1,10)=0.874
5F	Two Way RM ANOVA	GC=12 SGC=12	Number of Cells from 8 Animals (GC & SGC), 12 Recordings	Black Circles and Red Triangles: Average Error Bars: S.E.M.	0.049	F(1,11)=4.913
7D	Student's T-Test (Paired)	GC=8 SGC=8	Number of Cells from 6 Animals (GC & SGC)	Black Circles and Triangles: Average Error Bars : S.E.M.	GC: 0.434 SGC: 0.015	N/A